

# Achieving low noise in scanning tunneling spectroscopy F

Cite as: Rev. Sci. Instrum. **90**, 101401 (2019); <https://doi.org/10.1063/1.5111989>

Submitted: 31 May 2019 . Accepted: 09 September 2019 . Published Online: 02 October 2019

Jian-Feng Ge , Maoz Ovadia, and Jennifer E. Hoffman 

## COLLECTIONS

F This paper was selected as Featured



View Online



Export Citation



CrossMark

## ARTICLES YOU MAY BE INTERESTED IN

[The qPlus sensor, a powerful core for the atomic force microscope](#)



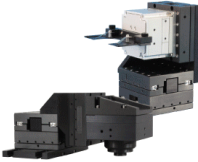
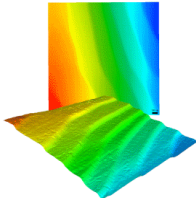
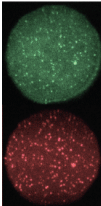
Review of Scientific Instruments **90**, 011101 (2019); <https://doi.org/10.1063/1.5052264>

[Design and analysis of the Tesla transformer with duplex secondary winding](#)

Review of Scientific Instruments **90**, 106104 (2019); <https://doi.org/10.1063/1.5123190>

[A high-pressure x-ray photoelectron spectroscopy instrument for studies of industrially relevant catalytic reactions at pressures of several bars](#)

Review of Scientific Instruments **90**, 103102 (2019); <https://doi.org/10.1063/1.5109321>

 <b>MCL</b> MAD CITY LABS INC. <a href="http://www.madcitylabs.com">www.madcitylabs.com</a>	<p>Nanopositioning Systems</p> 	<p>Modular Motion Control</p> 	<p>AFM and NSOM Instruments</p> 	<p>Single Molecule Microscopes</p> 
---	--	--	---	--

# Achieving low noise in scanning tunneling spectroscopy

Cite as: Rev. Sci. Instrum. 90, 101401 (2019); doi: 10.1063/1.5111989

Submitted: 31 May 2019 • Accepted: 9 September 2019 •

Published Online: 2 October 2019



View Online



Export Citation



CrossMark

Jian-Feng Ge,<sup>a)</sup>  Maoz Ovadia, and Jennifer E. Hoffman<sup>b)</sup> 

## AFFILIATIONS

Department of Physics, Harvard University, Cambridge, Massachusetts 02138, USA

<sup>a)</sup> [gejianfeng305@gmail.com](mailto:gejianfeng305@gmail.com)

<sup>b)</sup> [jhoffman@physics.harvard.edu](mailto:jhoffman@physics.harvard.edu)

## ABSTRACT

Scanning tunneling microscopy/spectroscopy (STM/S) is a powerful experimental tool to understand the electronic structure of materials at the atomic scale, with energy resolution down to the microelectronvolt range. Such resolution requires a low-vibration laboratory, low-noise electronics, and a cryogenic environment. Here, we present a thorough enumeration and analysis of various noise sources and their contributions to the noise floor of STM/S measurements. We provide a comprehensive recipe and an interactive python notebook to input and evaluate noise data, and to formulate a custom step-by-step approach for optimizing the signal-to-noise ratio in STM/S measurements.

Published under license by AIP Publishing. <https://doi.org/10.1063/1.5111989>

## I. INTRODUCTION

Scanning tunneling microscopy (STM) measures the net electric current  $I$  across a voltage-biased tunnel junction by bringing a sharp metallic tip into atomic-scale proximity with a sample. In the simplest mode of STM imaging, a feedback loop is used to maintain a constant tunneling current, by tracing out the atomic-scale topographical contours of the sample surface. The tunneling current is typically proportional to the energy-integrated density of states (DOS) of the sample surface, and thus scanning tunneling spectroscopy (STS) was suggested<sup>1</sup> and carried out<sup>2</sup> soon after the invention of STM. By STS, one can acquire the differential conductance  $g(V) = dI/dV$  as the sample energy probed (eV) is tuned by bias voltage ( $V$ ), with resolution reaching the microvolt range. A spatial map of  $g(\mathbf{r}, V)$  can be generated by raster scanning ( $x, y$ ) on the surface and sweeping  $V$  at each pixel.

Momentum resolution can be achieved by Fourier transform (FT) of a  $g(\mathbf{r}, V)$  map where surface imperfections cause quasiparticle scattering, yielding DOS as a function of in-plane momentum and energy  $\tilde{g}(\mathbf{q}, V)$ .<sup>3,4</sup> Here, the momentum  $\mathbf{q}$  is the difference of initial and final momenta  $\mathbf{k}_i$  and  $\mathbf{k}_f$  of a scattered quasiparticle. This technique, referred to as quasiparticle interference (QPI) imaging, enables observation of the local electronic band structure of the crystal surface. QPI imaging has been widely implemented in condensed

matter physics research, including high-temperature superconductivity,<sup>5–8</sup> heavy fermion compounds,<sup>9–11</sup> graphene,<sup>12</sup> and topological materials.<sup>13–16</sup> While direct observation of the surface electronic band structure is achievable by angle-resolved photoemission spectroscopy (ARPES), it is typically limited to occupied states (unless a delicate optical pump-probe setup is implemented<sup>17–19</sup>) and its spatial resolution is restricted by its optical wavelength (a few hundred nanometers). As a consequence, ARPES may inadvertently average multiple band structure signals from different domains or phases. On the other hand, QPI imaging can achieve spatial resolution down to the Fermi wavelength (typically a few nanometers) and can access unoccupied states simply by applying a positive sample bias voltage. Moreover, QPI can be used to image band structure dependence on the magnetic field, which is impossible with ARPES.

Time is the major limiting factor for high-resolution QPI imaging. First, a large real space area is required to maximize the QPI momentum resolution. Momentum resolution in ARPES is on the order of  $10^{-2} \text{ \AA}^{-1}$ ,<sup>20,21</sup> which equates to around 70 nm in real space. Second, high spatial resolution is required to compensate for the inevitable thermal drift caused by minute, time-dependent temperature gradients between tip and sample. Thermal drift leads to offsets in the spatial registration of individual spectra, which degrades the momentum resolution. If the drift is less than  $\sim 1 \text{ \AA}/h$  and the image

is acquired with atomic resolution in real space, then the Bragg peaks in the FT can serve as an exact length reference to correct the in-plane drift down to the picometer scale.<sup>22,23</sup>

As a concrete example of QPI parameters, in order to achieve a momentum resolution of  $10^{-2} \text{ \AA}^{-1}$ , an area as large as  $\sim 70 \text{ nm} \times 70 \text{ nm}$  is necessary. Additionally, a grid with  $256 \times 256$  points is desired to obtain atomic resolution in the  $70 \text{ nm} \times 70 \text{ nm}$  area (in-plane lattice constant is 3–6 Å for common materials) such that the whole Brillouin zone can be captured in the  $\tilde{g}(\mathbf{q}, V)$  map. To obtain 1 meV energy resolution in a 0.1 eV energy window then requires  $256 \times 256 \times 100 = 6.55 \times 10^6$  distinct measurements. As the holding time of a cryostat at base temperature typically varies from 50–200 h, this allows only 25–100 ms to ramp, settle, and integrate for each measurement. Therefore, it is crucial to improve the signal-to-noise ratio (SNR), defined as the ratio of the mean value to the standard deviation of the measured signal of interest  $X(t)$ ,

$$\text{SNR} = \frac{X_s}{\sqrt{\frac{1}{t_0} \int_0^{t_0} [X(t) - X_s]^2 dt}}, \quad (1)$$

where  $t_0$  is the duration of the measurement and  $X_s = \frac{1}{t_0} \int_0^{t_0} X(t) dt$  is the mean value of the measured signal as  $t_0 \rightarrow \infty$ . The denominator in Eq. (1) is the square root of the noise power,

$$P_{\text{noise}} = \frac{1}{t_0} \int_0^{t_0} [x(t)]^2 dt, \quad (2)$$

where  $x(t) = X(t) - X_s$  is the noise.<sup>24</sup> Generally, if the SNR of a single spectrum increases by a factor of 2, then it takes approximately  $1/\sqrt{2}$  of the measurement time to achieve the same result. With this time saving, one could increase the energy window, increase the energy resolution, or increase the momentum resolution by expanding the scan area if surface conditions allow.

The remainder of this review is organized as follows: In Sec. II, we establish a general formula for the SNR of STS using the homodyne (“lock-in”) method to measure differential conductance. We also discuss the choice of the low-pass filters (LPFs) for lock-in detection. In Sec. III, we introduce a toy model for noise and then demonstrate its application using our STM data. In Sec. IV, we discuss in detail three fundamental noise sources (transimpedance preamplifier noise, tunnel junction noise, and tip-sample distance modulation noise) and solutions to minimize them. Finally, in Sec. V, we summarize and give a practical step-by-step algorithm, supported by our open-source code, at <https://github.com/Let0n/achievinglownoiseinsts>, to optimize the SNR in its own STS and QPI measurements. The reader is encouraged to follow all analyses using the comprehensive example code provided<sup>25</sup> and to input his or her own noise data in order to attain specific recommendations to optimize an STM system.

## II. SIGNAL-TO-NOISE RATIO IN SCANNING TUNNELING SPECTROSCOPY

There are two methods to perform STS, namely, the DC method and the lock-in method. In the DC method, bias voltage  $V_{\text{dc}}$  is swept in the energy range of interest and DC current  $I_{\text{dc}}$  is

recorded at each point. Then, first-order numerical differentiation is applied to the  $I_{\text{dc}}(V)$  curve to obtain  $g(V)$ . In the lock-in method, an AC voltage excitation with a small amplitude  $V_{\text{ac}}$  at some frequency  $f_0$  is added to a DC voltage sweep, then the AC current amplitude  $I_{\text{ac}}$  at the same frequency  $f_0$  is measured by a lock-in amplifier. Differential conductance  $g(V)$  is then a simple division of  $I_{\text{ac}}/V_{\text{ac}}$ .

Because STM works at an ultralow current range on the order of  $10^{-12} \text{ A}$ , we read out tunneling current with the aid of a transimpedance amplifier (TIA) (often referred to as a “preamplifier”), which converts current to voltage. All the information, including both signal and noise, is contained in the output. To discern different noise components, it is more constructive to look at the frequency domain of the output (using a spectrum analyzer) than time domain (using an oscilloscope). Therefore, we rewrite Eq. (1) in the frequency domain,

$$\text{SNR} = \left[ \frac{X_s^2}{\int_{-\infty}^{\infty} |x(f)|^2 df} \right]^{1/2}, \quad (3)$$

where the Fourier transform takes the form of  $x(f) = \frac{1}{\sqrt{t_0}} \int_0^{t_0} e^{-2\pi i f t} x(t) dt$ .<sup>26</sup> We use  $j$  as the imaginary unit to distinguish it from the noise current  $i$  introduced later.

Figure 1 shows a schematic of the typical noise power spectral density (PSD) of the STM tunneling current measured by a preamplifier, which is composed of three parts:

1. Flicker noise dominates from DC up to a corner frequency  $f_F$ . The PSD of flicker noise can be expressed<sup>27</sup> as  $K_F I^2 / f$ , where  $K_F$  is an empirical coefficient, so the flicker noise is also known as “ $1/f$  noise.” The origin of flicker noise has been attributed to mobility fluctuations or charge trapping in electronic devices.<sup>27,28</sup>
2. The middle-frequency range extending from  $f_F$  to the bandwidth of the preamplifier is typically relatively flat and primarily from the Johnson-Nyquist current noise. We will discuss the composition of preamplifier noise current PSD  $S_{\text{aa}}(f)$  in Sec. IV A. The corner frequency of flicker noise  $f_F$  varies with tunneling current and can be determined by  $K_F I^2 / f_F = S_{\text{aa}}(f_F)$ .

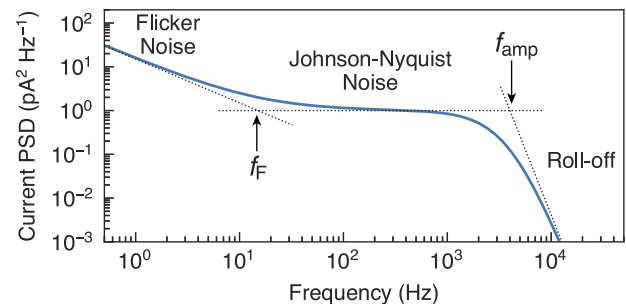


FIG. 1. An illustrative example of typical noise current PSD of a STM tunnel junction. The corner frequency of Flicker noise is labeled  $f_F$ . The bandwidth of the preamplifier,  $f_{\text{amp}}$ , is 4 kHz in this example.

3. A preamplifier has a second- or higher-order low-pass filter (LPF) with a cutoff frequency  $f_{\text{amp}}$ , so noise at frequencies above  $f_{\text{amp}}$  is heavily suppressed. The LPF of the preamplifier acts on the signal as well, so the signal is also suppressed above  $f_{\text{amp}}$ .

From Fig. 1, we can see that the noise spectral density is lower in the middle frequency range, where the signal is not yet attenuated by the cutoff frequency  $f_{\text{amp}}$ . Generally, it is more advantageous to use the lock-in method with a frequency in this middle-frequency range than the DC method to optimize the SNR when flicker noise dominates in the low frequency range.<sup>29–31</sup> Specifically, the lock-in method will give a higher SNR than the DC method when flicker noise power  $P_F$  is larger than preamplifier noise power  $P_{\text{amp}}$ ,

$$P_F = \int_{f_{\text{meas}}}^{f_F} K_F \frac{I^2}{f} df > P_{\text{amp}} = \int_0^{f_{\text{amp}}} S_{\text{aa}}(f) df, \quad (4)$$

where  $S_{\text{aa}}(f)$  will be quantified in Eq. (52) and the lower bound  $f_{\text{meas}} \sim (2\pi t_{\text{meas}})^{-1}$  is the frequency associated with the time scale of a single measurement  $t_{\text{meas}}$ . In practice, one can measure the current noise PSD with sufficient frequency resolution to fit the values of  $K_F$  and  $f_F$ , then compare flicker noise power with preamplifier noise power to determine which method should be used in spectroscopy. Except in rare cases, flicker noise dominates, so hereafter we will focus on the more advantageous lock-in method for spectroscopic measurements.

### A. Tunneling spectroscopy with a lock-in amplifier

Homodyne detection is commonly carried out by a lock-in amplifier. A lock-in amplifier performs a multiplication (demodulation) of its input (transimpedance-amplified tunneling current) with the reference signal (bias modulation) and then applies a low-pass filter to the product to recover the signal at the modulation frequency. As shown in the circuit diagram in Fig. 2(a), a spectroscopic measurement is performed by applying a DC voltage bias  $V_{\text{dc}}$  and AC voltage modulation  $V_{\text{ac}}$  to the tunnel junction at frequency  $f_0$ . For a tunnel junction with a current-to-voltage relation  $I(V)$ , at small enough  $V_{\text{ac}}$ , a Taylor expansion gives the resulting current,

$$I(t) = I(V_{\text{dc}}) + g(V_{\text{dc}})V_{\text{ac}} \cos(2\pi f_0 t) + i_j(t) + i_a(t), \quad (5)$$

where the last two terms are additive noise due to the current fluctuations in the tunnel junction  $i_j(t)$  and the noise of the preamplifier  $i_a(t)$ . In Eq. (5), the first three terms  $I(V_{\text{dc}})$ ,  $g(V_{\text{dc}})$ , and  $i_j(t)$  are defined at the average tip-to-sample distance  $z_0$ . Tunneling current is actually proportional to  $e^{-\kappa z(t)}$ , where  $\kappa^{-1}$  is the current decay length, so we need to multiply the first three terms in Eq. (5) by a factor of  $e^{-\kappa z(t)}$ . If we write  $z(t) = z_0 - z_n(t)$ , where  $z_n(t)$  is the disturbance in the tip-sample distance, then we can approximate Eq. (5) to first order, assuming  $\kappa z_n \ll 1$  and neglecting second- and higher-order terms

$$\begin{aligned} I(t) &= [I(V_{\text{dc}}) + g(V_{\text{dc}})V_{\text{ac}} \cos(2\pi f_0 t) + i_j(t)] \times e^{\kappa z_n(t)} + i_a(t) \\ &\approx [I(V_{\text{dc}}) + g(V_{\text{dc}})V_{\text{ac}} \cos(2\pi f_0 t)] \times [1 + \kappa z_n(t)] \\ &\quad + i_j(t) + i_a(t). \end{aligned} \quad (6)$$

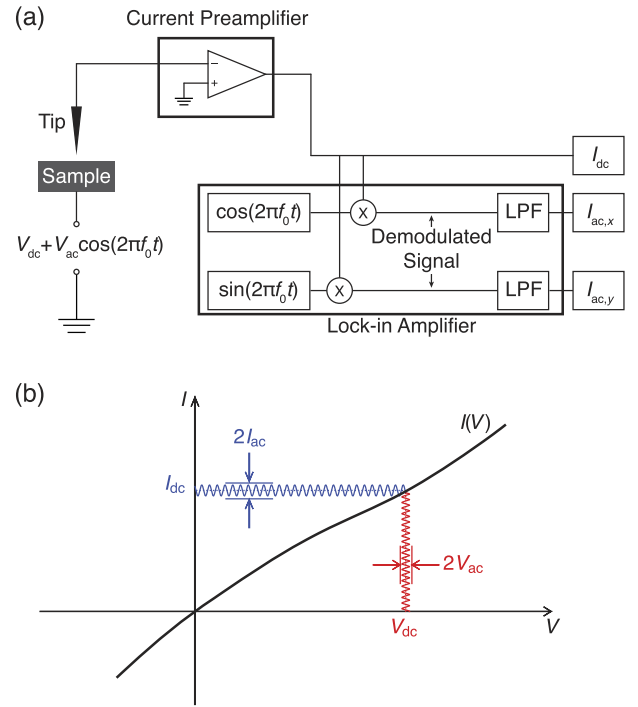


**FIG. 2.** Tunneling spectroscopy with a lock-in amplifier. (a) A circuit diagram of a spectroscopic measurement with a modulation frequency  $f_0$ .  $I_{\text{ac},x}$  and  $I_{\text{ac},y}$  are two orthogonal components of the demodulation signal  $I_{\text{ac}}^2 = I_{\text{ac},x}^2 + I_{\text{ac},y}^2$ . (b) An example  $I(V)$  curve (black) showing modulation and demodulation in the lock-in method. At each point of the curve (black) that arises from sample characteristics, a bias modulation (red) with a peak amplitude of  $V_{\text{ac}}$  is superimposed on a DC bias voltage  $V_{\text{dc}}$ . The resulting current (blue) has a DC value of  $I_{\text{dc}}$  and an AC component with a peak amplitude of  $I_{\text{ac}}$ . The derived  $g(V)$  spectrum is shown in Fig. 3(a).

For simplicity, we can rewrite it as

$$I(t) = [I_{\text{dc}} + I_{\text{ac}} \cos(2\pi f_0 t)] \times [1 + \zeta(t)] + i_j(t) + i_a(t), \quad (7)$$

where

$$I_{\text{dc}} \equiv I(V_{\text{dc}}), \quad (8a)$$

$$I_{\text{ac}} \equiv g(V_{\text{dc}})V_{\text{ac}}, \quad (8b)$$

$$\zeta(t) \equiv \kappa z_n(t). \quad (8c)$$

Note that  $\zeta(t)$  is a dimensionless function that quantifies the modulation of the instantaneous tunneling current by fluctuations in the tip-sample distance  $z(t)$ . For example, if the current at  $z = z_0$  is equal to  $I_0$ , then  $I(t) = I_0[1 + \zeta(t)]$ .

The lock-in amplifier first removes the DC component in Eq. (7) via a high-pass filter (which usually has a cutoff frequency less than 1 Hz), then the remaining AC signal is demodulated by multiplying by  $\cos(2\pi f_0 t)$ .<sup>32</sup> The resulting demodulated signal<sup>33</sup> [Fig. 2(a)] is proportional to the sum of the “noise-free” signal  $X_s = I_{\text{ac}}$  and the noise current  $x(t) = i(t)$ ,

$$\begin{aligned}
 [I(t) - I_{dc}] \cos(2\pi f_0 t) &= I_{ac} \cos^2(2\pi f_0 t) + I_{ac} \zeta(t) \cos^2(2\pi f_0 t) \\
 &\quad + [I_{dc} + i_j(t)\zeta(t) + i_a(t)] \cos(2\pi f_0 t) \\
 &= \frac{1}{2} \{ I_{ac} + I_{ac} \zeta(t) + 2[I_{dc} \zeta(t) + i_j(t) + i_a(t)] \\
 &\quad \times \cos(2\pi f_0 t) + I_{ac} [1 + \zeta(t)] \cos(4\pi f_0 t) \}.
 \end{aligned} \tag{9}$$

Therefore,

$$\begin{aligned}
 i(t) &= I_{ac} \zeta(t) + 2[I_{dc} \zeta(t) + i_j(t) + i_a(t)] \cos(2\pi f_0 t) \\
 &\quad + I_{ac} [1 + \zeta(t)] \cos(4\pi f_0 t).
 \end{aligned} \tag{10}$$

We then transform Eq. (10) to the frequency domain to analyze noise contributions. The Fourier transform of a product of two functions is equal to the convolution of their Fourier transforms. The Fourier transform of the cosine function is a pair of Dirac  $\delta$ -functions, so their convolution with other functions is especially simple

$$\begin{aligned}
 i(f) &= I_{ac} \zeta(f) + 2[I_{dc} \zeta(f) + i_j(f) + i_a(f)] * \frac{1}{2} [\delta(f - f_0) + \delta(f + f_0)] \\
 &\quad + I_{ac} [1 + \zeta(f)] * \frac{1}{2} [\delta(f - 2f_0) + \delta(f + 2f_0)] \\
 &= I_{ac} \zeta(f) + I_{dc} [\zeta(f - f_0) + \zeta(f + f_0)] + [i_a(f - f_0) + i_a(f + f_0)] \\
 &\quad + [i_j(f - f_0) + i_j(f + f_0)] + \frac{1}{2} I_{ac} [\zeta(f - 2f_0) + \zeta(f + 2f_0)] \\
 &\quad + \frac{1}{2} I_{ac} [\delta(f - 2f_0) + \delta(f + 2f_0)].
 \end{aligned} \tag{11}$$

The noise PSD is given by

$$S_{ii}(f) = i(f) i^*(f), \tag{12}$$

where  $i^*(f)$  denotes the complex conjugate of  $i(f)$ . The noise PSD contains

1. autocorrelation terms such as  $\zeta(f)\zeta^*(f)$  and  $\zeta(f - 2f_0)\zeta^*(f - 2f_0)$ ,
2. cross-correlation terms between two different functions, such as  $\zeta(f - f_0)i_a^*(f - f_0)$  and  $\zeta(f - 2f_0)\delta^*(f - 2f_0)$ ,
3. cross-correlation terms between the same function with different frequency shifts, such as  $\zeta(f - f_0)\zeta^*(f - 2f_0)$ .

The cross correlation between two different random functions, when averaged across multiple realizations, is zero if their respective processes are uncorrelated. The terms  $i_a$ ,  $i_j$ , and  $\zeta$  are completely uncorrelated with each other, so their cross-correlation terms can be dropped. Similarly, the correlation between two frequency-shifted versions of  $i_a$  or  $i_j$ , dominated by flicker noise or the Johnson-Nyquist current noise, is zero. However, it is not clear if terms such as  $\zeta(f - f_0)\zeta^*(f - 2f_0)$  can be dropped because the physical components that cause the vibration noise may have harmonics that lead to a nonzero cross correlation between frequency-shifted versions of  $\zeta$ . In what follows we assume that all cross-correlation terms are negligible. It is a good approximation as long as we choose a modulation frequency  $f_0$  such that both  $f_0$  and  $2f_0$  are away from mechanical or electrical resonances of the system and environment [so cross-correlation terms such as  $\zeta(f - 2f_0)\delta^*(f - 2f_0)$  vanish]. We also show an example in Fig. 24 in the Appendix that the estimated

lock-in demodulation current PSD under this approximation still agrees quite well with the measured result.

Defining

$$S_{\zeta\zeta}(f) = \zeta(f)\zeta^*(f), \tag{13a}$$

$$S_{aa}(f) = i_a(f)i_a^*(f), \tag{13b}$$

$$S_{jj}(f) = i_j(f)i_j^*(f), \tag{13c}$$

we can write the total PSD as the sum of all PSDs of the individual terms of  $i(f)$ ,<sup>34</sup>

$$\begin{aligned}
 S_{ii}(f) &= I_{ac}^2 S_{\zeta\zeta}(f) + I_{dc}^2 [S_{\zeta\zeta}(f - f_0) + S_{\zeta\zeta}(f + f_0)] \\
 &\quad + [S_{aa}(f - f_0) + S_{aa}(f + f_0)] + [S_{jj}(f - f_0) + S_{jj}(f + f_0)] \\
 &\quad + \frac{1}{4} I_{ac}^2 [S_{\zeta\zeta}(f - 2f_0) + S_{\zeta\zeta}(f + 2f_0)] \\
 &\quad + \frac{1}{4} I_{ac}^2 [\delta(f - 2f_0) + \delta(f + 2f_0)].
 \end{aligned} \tag{14}$$

To make this notation more compact, we define the modulated noise PSDs

$$S_{\zeta\zeta,f_0} \equiv \frac{1}{2} [S_{\zeta\zeta}(f - f_0) + S_{\zeta\zeta}(f + f_0)], \tag{15a}$$

$$S_{aa,f_0} \equiv \frac{1}{2} [S_{aa}(f - f_0) + S_{aa}(f + f_0)], \tag{15b}$$

$$S_{jj,f_0} \equiv \frac{1}{2} [S_{jj}(f - f_0) + S_{jj}(f + f_0)], \tag{15c}$$

$$S_{\delta\delta,2f_0} \equiv \frac{1}{2} [\delta(f - 2f_0) + \delta(f + 2f_0)], \tag{15d}$$

so that the total current PSD of the demodulated signal becomes

$$S_{ii} = I_{ac}^2 S_{\zeta\zeta,0} + 2I_{dc}^2 S_{\zeta\zeta,f_0} + 2S_{aa,f_0} + 2S_{jj,f_0} + \frac{1}{2} I_{ac}^2 S_{\zeta\zeta,2f_0} + \frac{1}{2} I_{ac}^2 S_{\delta\delta,2f_0}, \tag{16}$$

which can be compared with the signal power  $I_{ac}^2$ .

During a spectroscopic measurement,  $I_{ac}$  is generally not a constant but is typically bounded, whereas  $I_{dc}$  is assumed to be a monotonic function of  $V_{dc}$  that typically reaches values much larger than  $I_{ac}$ . It is interesting, therefore, to note the dependence of the different noise contributions on the ratio  $I_{dc}/I_{ac}$ ,

$$\begin{aligned}
 S_{ii}/I_{ac}^2 &= S_{\zeta\zeta,0} + \frac{S_{\zeta\zeta,2f_0}}{2} + \frac{S_{\delta\delta,2f_0}}{2} + \frac{2S_{aa,f_0}}{I_{ac}^2} + \frac{2S_{jj,f_0}}{I_{ac}^2} + 2S_{\zeta\zeta,f_0} \left( \frac{I_{dc}}{I_{ac}} \right)^2 \\
 &= S_{\zeta\zeta,0} + \frac{S_{\zeta\zeta,2f_0}}{2} + \frac{S_{\delta\delta,2f_0}}{2} + \frac{2S_{aa,f_0}}{I_{ac}^2} + \frac{2k_B T}{R_j I_{ac}^2} \\
 &\quad + \frac{2e}{I_{ac}} \left( \frac{I_{dc}}{I_{ac}} \right) + 2S_{\zeta\zeta,f_0} \left( \frac{I_{dc}}{I_{ac}} \right)^2,
 \end{aligned} \tag{17}$$

where we have approximated the junction noise  $S_{jj,f_0}$  as the sum of the Johnson-Nyquist current noise and shot noise components (we will discuss them in detail in Sec. IV B). Apparently, there are terms independent of  $I_{dc}/I_{ac}$ , one term linear in  $I_{dc}/I_{ac}$ , and one term quadratic in  $I_{dc}/I_{ac}$  that gradually dominates the noise spectrum as the bias voltage is increased.

In order to calculate the output noise power  $P_{noise}$  from the demodulated noise current PSD  $S_{ii}$ , we must take into account the



output LPF of the lock-in amplifier. The lock-in amplifier LPF has a transfer function  $H(f)$ , giving

$$\begin{aligned} P_{\text{noise}} &= \int_{-\infty}^{\infty} [H(f)i(f)][H(f)i(f)]^* df \\ &= \int_{-\infty}^{\infty} S_{ii}(f)|H(f)|^2 df. \end{aligned} \quad (18)$$

We define four dimensionless specific noise power

$$p_{\zeta\zeta,0} = \int_{-\infty}^{\infty} S_{\zeta\zeta,0}|H(f)|^2 df, \quad (19a)$$

$$p_{\zeta\zeta,f_0} = \int_{-\infty}^{\infty} S_{\zeta\zeta,f_0}|H(f)|^2 df, \quad (19b)$$

$$p_{\zeta\zeta,2f_0} = \int_{-\infty}^{\infty} S_{\zeta\zeta,2f_0}|H(f)|^2 df, \quad (19c)$$

$$p_{\delta\delta,2f_0} = \int_{-\infty}^{\infty} S_{\delta\delta,2f_0}|H(f)|^2 df = |H(2f_0)|^2, \quad (19d)$$

and two current noise power

$$P_{aa,f_0} = \int_{-\infty}^{\infty} S_{aa,f_0}|H(f)|^2 df, \quad (20a)$$

$$P_{jj} = \int_{-\infty}^{\infty} S_{jj}|H(f)|^2 df = 2S_{jj}B_N. \quad (20b)$$

We will discuss the frequency dependence of  $S_{aa,f_0}$  in Sec. IV A, while in Eq. (20b), we use the fact that  $S_{jj}$  is frequency independent (see Sec. IV B), and  $B_N = \int_0^\infty |H(f)|^2 df$  is the equivalent noise bandwidth (ENBW) of the LPF of the lock-in amplifier assuming a passband gain of 1. We can finally obtain the SNR as

$$\begin{aligned} \text{SNR} = \frac{I_{ac}}{\sqrt{P_{\text{noise}}}} &= \left[ p_{\zeta\zeta,0} + 2\left(\frac{I_{dc}}{I_{ac}}\right)^2 p_{\zeta\zeta,f_0} + \frac{2P_{aa,f_0}}{I_{ac}^2} + \frac{2P_{jj}}{I_{ac}^2} \right. \\ &\left. + \frac{1}{2}p_{\zeta\zeta,2f_0} + \frac{1}{2}|H(2f_0)|^2 \right]^{-1/2}. \end{aligned} \quad (21)$$

Commonly, the SNR is expressed in decibels

$$\begin{aligned} \text{SNR[dB]} &= 20 \log_{10} \left( \frac{I_{ac}}{\sqrt{P_{\text{noise}}}} \right) \\ &= -10 \log_{10} \left[ p_{\zeta\zeta,0} + 2\left(\frac{I_{dc}^2}{I_{ac}^2}\right) p_{\zeta\zeta,f_0} + \frac{2P_{aa,f_0}}{I_{ac}^2} + \frac{2P_{jj}}{I_{ac}^2} \right. \\ &\quad \left. + \frac{1}{2}p_{\zeta\zeta,2f_0} + \frac{1}{2}|H(2f_0)|^2 \right]. \end{aligned} \quad (22)$$

For example, an SNR of 40 dB means that the root-mean-square (rms) noise amplitude is 1% of the signal.

Equation (22) gives a mathematical expression to calculate the SNR from specific noise sources. Practically, the SNR can also be estimated as the mean value of  $g(V)$  divided by the standard deviation of  $g(V)$  from multiple spectra because  $g \times V_{ac} = I_{ac}$ , and the standard deviation of  $I_{ac}$  is equal to  $\sqrt{P_{\text{noise}}}$  (square root of frequency-integrated PSD). We show in Fig. 3 the relation between SNR in direct measured  $g(V)$  spectra and SNR derived from current noise PSD out of the lock-in amplifier [i.e., from Eq. (22)]. The fluctuations in single spectra (red) in Fig. 3(a) indicate visually the rms noise amplitude compared to the signal (the black average curve). To clarify the simple relationship between  $I_{ac}$  and  $g$ , we note the measured  $I_{ac} = 13.8$  pA at  $V_{dc} = 0.40$  V yields  $g(0.4 \text{ V}) = 2.76$  nA/V. At  $V_{dc} = 0.40$  V,  $g = 2.771 \pm 0.065$  nA/V, and thus the SNR estimated from 100 bias spectra in Fig. 3(a) is 32.6 dB. On the other hand, integrating Fig. 3(c) from 5 Hz to 5 kHz gives  $\sqrt{P_{\text{noise}}}$  of 0.38 pA, which yields a SNR of 31.9 dB using Eq. (22). Therefore, the estimation of the SNR from multiple spectra taken at identical conditions agrees well with the SNR derived from Eq. (22). We also note that the standard deviation of  $g(V)$  increases with increasing  $|I_{dc}|$  in Fig. 3(b), indicating a smaller SNR with a higher tunneling current.

We pause at this point to inspect the different factors that influence the SNR

1. The LPF of the lock-in amplifier with the transfer function  $|H(f)|$  is selected by the experimenter. We will discuss the choice of LPF in Sec. II B.

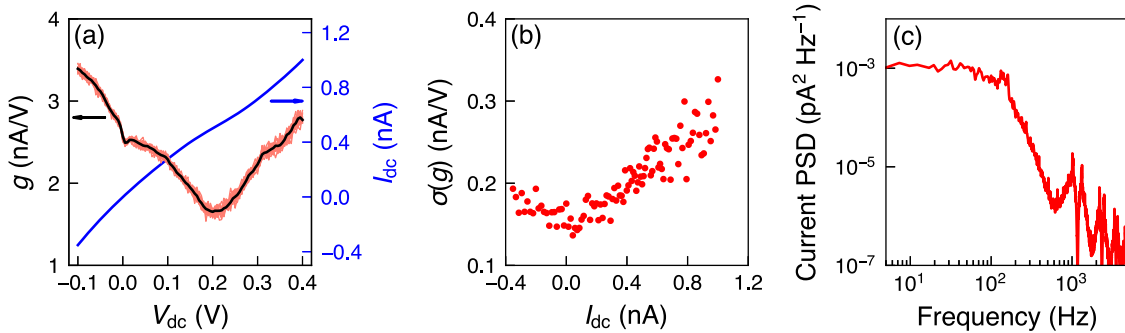


**FIG. 3.** Illustration of SNR in terms of bias spectroscopy and frequency spectroscopy. (a) Average bias spectrum  $g(V)$  (black) of 100 spectra [20 randomly selected single spectra are shown (red)] taken with the same setup conditions of  $V_{dc} = 0.40$  V,  $I_{dc} = 1.0$  nA measured on a cleaved semimetal CeBi surface at 4 K. A bias modulation with frequency  $f_0 = 1.17$  kHz and  $V_{ac} = 5$  mV was applied. Simultaneously taken  $I_{dc}(V)$  (blue) is shown to convert from  $V_{dc}$  to  $I_{dc}$ . (b) Standard deviation of differential conductance  $\sigma(g)$  in (a) shows an increasing trend with increasing  $|I_{dc}|$ . (c) Current power spectral density of the lock-in output  $S_{ii}|H(f)|^2$  as a function of frequency. The frequency spectrum was measured with the same setup conditions  $V_{dc} = 0.40$  V,  $I_{dc} = 1.0$  nA immediately before the bias spectroscopic measurement in (a), with the same bias modulation applied. A boxcar (“synchronous”) filter at settling time  $t_s = (2\pi f_0)^{-1}$  and then a second-order RC filter with  $t_s = 10$  ms were applied for both measurements in (a) and (b). The choice of low-pass filters will be discussed in Sec. II B.

- $I_{dc}$  is determined by the sample properties, DC bias voltage  $V_{dc}$ , and average tip-sample separation  $z_0$ . Within a few constraints such as the current resolution and limits of the preamplifier, the experimenter can select any  $z_0$ .
- $I_{ac}$  is determined by the sample properties, voltage modulation  $V_{ac}$ , and the junction impedance  $dV/dI$
- $V_{ac}$  is selected by the user and determines the energy resolution of the measurement when thermal broadening can be neglected, i.e., when  $eV_{ac} \gg 2k_B T_j$ .<sup>35</sup>
- $S_{aa}$  is determined by the preamplifier noise and may depend on the input impedance (including tunnel junction and cable impedance)  $dV/dI$ . We will discuss  $S_{aa}$  in Sec. IV A.
- $S_{jj}$  is composed of the junction Johnson-Nyquist current noise proportional to junction temperature, and shot noise proportional to  $I_{dc}$ . We will discuss  $S_{jj}$  in Sec. IV B.
- $S_{\zeta\zeta}$  is determined by environmental vibrations and STM stiffness, by scan voltage noise and scanner response, and by the electronic properties of the tip and sample that determine  $\kappa$ . We will discuss  $S_{\zeta\zeta}$  in Sec. IV C.

The SNR may vary by over 10 dB at different  $I_{dc}$  values within a single spectroscopic measurement, as exemplified in Fig. 16. In order to optimize the efficiency in a spectroscopic measurement, we can keep the SNR approximately constant over the range of bias voltage either by increasing the number of averages  $N(V)$  with increasing  $|V|$ , which increases the SNR by  $10 \log_{10} N$  dB, or by adjusting  $H(f)$  as a function of  $V_{dc}$  as shown in Sec. III A.

To give a clear view of how each term in Eq. (21) contributes to the SNR, Fig. 4 illustrates the noise flow toward the output of

the lock-in amplifier. The prime feature of the noise flow is that the noise experiences two convolution operations (labeled by red asterisks in Fig. 4) in the frequency domain: the first one between dimensionless  $\zeta(f)$  and current (both signal and noise) before entering preamplifier input and the second one between the output of the preamplifier and the reference signal in the lock-in amplifier. The consequence of the convolution operations is exhibited in the terms involving the specific noise power of  $\zeta$  such as  $P_{\zeta\zeta, f_0}$  in Eq. (22).

### B. Choice of the low-pass filter for the lock-in amplifier

We will first discuss the choice of LPF for the lock-in amplifier since it is flexible to control. After the demodulation process in the lock-in amplifier [Eq. (9)], the signal  $I_{ac}$  to be measured at the output of the lock-in is the DC component. Even without external noise sources  $\zeta$ ,  $i_j$ ,  $i_a$  adding to the input of the lock-in amplifier, the demodulation also generates a  $2f_0$  component at the output with the same amplitude as the signal  $I_{ac}$ , as shown in Eq. (10). This  $2f_0$  component, along with interfering noise at other frequencies, must be filtered out to obtain the desired DC component  $I_{ac}$ . In order to select an optimal LPF for the lock-in amplifier, one must consider the following: (1) the filter frequency response  $|H(f)|^2$  and its equivalent noise bandwidth  $B_N$ . The smaller the  $B_N$ , the lower the output noise. (2) The filter step response or more specifically its settling time. The settling time determines how long one must wait after setting up the measurement parameters before a valid value appears at the output. These two factors are inversely related:

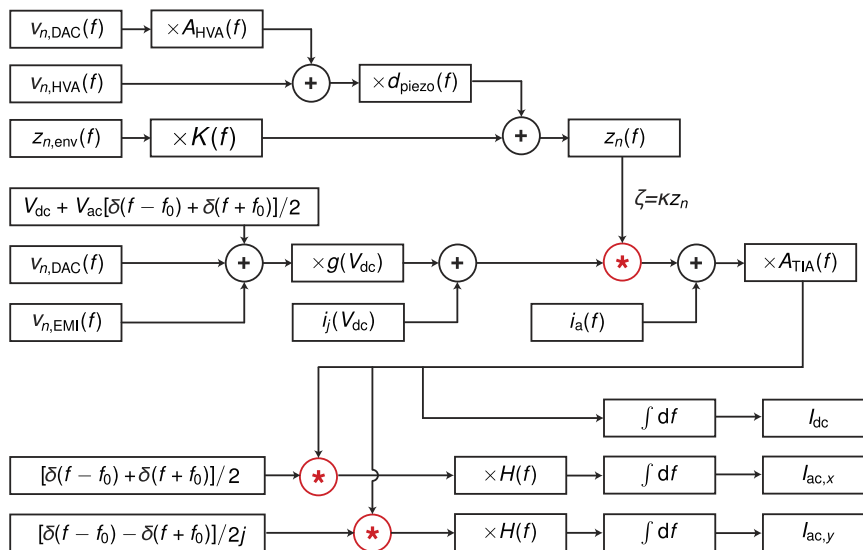


**FIG. 4.** The flowchart of signal and noise in the frequency domain in spectroscopic measurements with a lock-in amplifier. Voltage noise, current noise, and Z noise are denoted by  $v_n$ ,  $i$ , and  $z_n$ , respectively, while “env” is short for the environment. DAC stands for digital-to-analog converter. HVA stands for high voltage amplifier. EMI stands for electromagnetic interference.  $A_{HVA}$  and  $A_{TIA}$  denote the gains of the HVA and preamplifier.  $d_{piezo}$  is the piezoelectric coefficient (in the unit of m/V) of the z piezo scanner.  $K$  is the mechanical transfer function of the full STM system from external vibrations to the tip-sample distance. The plus operation means rms sum (the powers rather than the amplitudes are additive), while the asterisk operation means convolution.  $\int df$  is the integration to obtain the final results. The subscripts  $x$  and  $y$  are two orthogonal components of the primitive output of the lock-in amplifier, which are used to derive  $I_{ac}$  after adjusting the lock-in phase to remove the out-of-phase current that arises from capacitive coupling rather than tunneling.

a filter with small  $B_N$  will result in lower noise but will have a long settling time. A filter with a short settling time will have a large  $B_N$ .<sup>36</sup>

In the following, we compare two types of LPFs commonly used in lock-in detection. We use a continuous-time approximation, despite the fact that most lock-in amplifiers today measure digitally. This approximation is valid when the sampling frequency is much higher than the modulation frequency used.

### 1. *n*th-order RC filter

This type of filter is described by a time constant  $\tau$  and an order  $n$ , which is equal to the number of cascaded first-order RC filters. The frequency response function of the filter is

$$H(f) = \left( \frac{1}{1 + j2\pi f\tau} \right)^n. \quad (23)$$

This function can be integrated to obtain the noise bandwidth  $B_N$ ,

$$B_N = \frac{1}{2\pi\tau} \int_0^\infty \left( \frac{1}{1 + x^2} \right)^n dx = \frac{1}{4\sqrt{\pi}\tau} \frac{\Gamma(n - \frac{1}{2})}{\Gamma(n)}, \quad (24)$$

where  $\Gamma(n)$  is the Gamma function. This filter's time-domain response to a unit step function is described by the following equation:<sup>37</sup>

$$y(t) = \int_{-\infty}^\infty u(t)h(t - t')dt' = 1 - e^{-t/\tau} \sum_{l=0}^{n-1} \frac{1}{l!} \left( \frac{t}{\tau} \right)^l, \quad (25)$$

where  $u(t)$  is the unit step function and  $h(t)$  is the impulse response of the filter [inverse Laplace transform of Eq. (23)]. We define the settling time  $t_s$  by demanding that the filter output is within 0.1% of its asymptotic value, and therefore

$$1/1000 = e^{-t_s/\tau} \sum_{l=0}^{n-1} \frac{1}{l!} \left( \frac{t_s}{\tau} \right)^l. \quad (26)$$

Equation (26) can be solved easily for  $n = 1$  but requires a numerical solution for higher  $n$ . We show in Fig. 5 both the step response function  $y(t)$  and the filter response function  $|H(f)|^2$  of the RC filter with an order ranging from 1 to 8 for an equal settling time of 10 ms. The reader can play with the parameter  $\tau$  in our code<sup>25</sup> to determine the settling time when an RC filter is used for the lock-in amplifier in a spectroscopic measurement. For an equal time constant [Fig. 5(a)], a higher order RC filter requires more time to settle after encountering a step change in voltage during a spectroscopic measurement. On the other hand, a higher order RC filter has a lower noise bandwidth for an equal settling time [Fig. 5(b)]. The filter “efficiency” can be determined by the time-bandwidth product  $t_s B_N$ , with a lower product being better. Table 1 shows for different order  $n$ , the noise bandwidth  $B_N$ , the settling time  $t_s$ , the efficiency  $t_s B_N$ , and the filter attenuation  $|H(f)|^2$  at the high frequency limit, for a given time constant. It also suggests that it is preferable to select a filter of order  $n = 4$  or higher.

### 2. Boxcar filter (“synchronous filter”)

For the boxcar filter, the averaging time defines the settling time  $t_s = t_{\text{avg}}$ . The filter has a frequency response of

$$H(f) = \frac{\sin(\pi t_{\text{avg}} f)}{\pi t_{\text{avg}} f}. \quad (27)$$

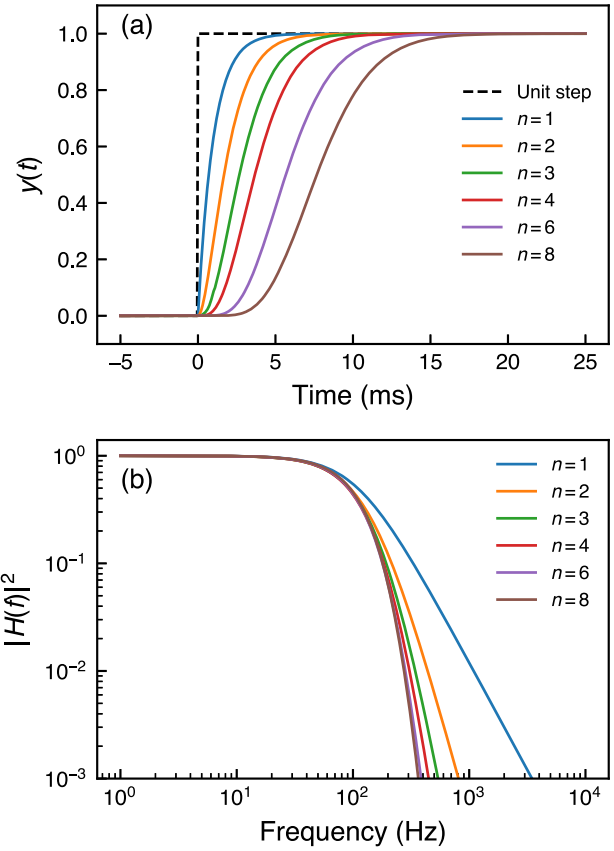


**FIG. 5.** Response characteristics of *n*th-order RC filter with different *n*. (a) Time-domain step response  $y(t)$  for different *n* with an equal time constant  $\tau = 1$  ms. The black dashed line presents an ideal unit step response as a reference. (b) Frequency-domain response function  $|H(f)|^2$  for different *n* with an equal settling time  $t_s = 10$  ms defined in Eq. (26).

Again, we perform an integration to determine the noise bandwidth of this filter

$$B_N = \int_0^\infty \left[ \frac{\sin(\pi t_{\text{avg}} f)}{\pi t_{\text{avg}} f} \right]^2 df = \frac{1}{2t_{\text{avg}}}. \quad (28)$$

**TABLE I.** Noise bandwidth  $B_N$ , settling time  $t_s$ , time-bandwidth product  $t_s B_N$ , and filter response function for RC filters with different order  $n$ , for a given filter time constant  $\tau$ .

$n$	$B_N$	$t_s$	$B_N t_s$	$ H(f) ^2$
1	$0.250\tau^{-1}$	$6.91\tau$	1.73	$(0.91t_s f)^{-2}$
2	$0.125\tau^{-1}$	$9.22\tau$	1.15	$(0.68t_s f)^{-4}$
3	$0.094\tau^{-1}$	$11.23\tau$	1.06	$(0.56t_s f)^{-6}$
4	$0.078\tau^{-1}$	$13.06\tau$	1.02	$(0.48t_s f)^{-8}$
6	$0.062\tau^{-1}$	$16.45\tau$	1.02	$(0.38t_s f)^{-12}$
8	$0.052\tau^{-1}$	$19.63\tau$	1.02	$(0.32t_s f)^{-16}$



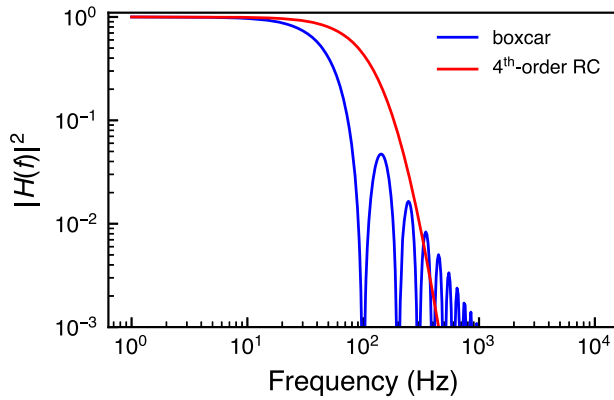


**FIG. 6.** Comparison of response function  $|H(f)|^2$  between a boxcar filter and a  $n$ th-order RC filter, with an equal settling time  $t_s = 10$  ms. The boxcar filter has an averaging time  $t_{\text{avg}}$  of 10 ms, while the RC filter has a time constant  $\tau$  of 0.763 ms.

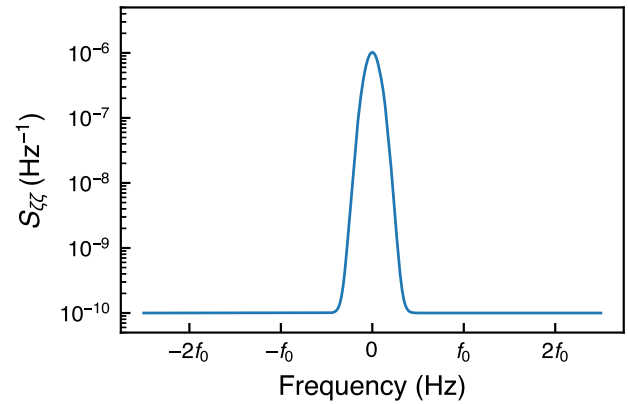


**FIG. 7.** The example PSD of dimensionless quantity  $\zeta$  used in the toy model. We take  $\zeta(f)$  in the Gaussian form of  $\zeta_c + \zeta(0)e^{-\frac{f^2}{2(f_0/10)^2}}$ , where  $\zeta_c = 10^{-5} \text{ Hz}^{-1/2}$  is the white noise background,  $\zeta(0) = 10^{-3} \text{ Hz}^{-1/2}$  is the amplitude of the Gaussian peak, and  $f_0$  is the modulation frequency.

The time-bandwidth product for this filter is therefore

$$t_s B_N = \frac{1}{2}, \quad (29)$$

which is lower than any RC filter. If the goal is to attain the lowest possible noise bandwidth within a given measuring time, then the boxcar filter is preferred. We give an example in Fig. 6, showing the comparison of response functions between a boxcar filter and a 4th-order RC filter with the same settling time of 10 ms. The  $-3$  dB bandwidth of the boxcar filter is 32.0 Hz, which is lower than that of the 4th-order RC filter, 62.4 Hz. We note that the response function of the boxcar filter has moderate high frequency “lobes,” which should be taken into account in lock-in measurements, as shown in Fig. 10.

### III. ANALYZING NOISE IN AN ACTUAL INSTRUMENT

#### A. Toy model

To illustrate the form of the noise spectrum in Eq. (16) and the resulting SNR in Eq. (21), we will take an example, assuming  $\zeta(f)$  is Gaussian noise with a peak power spectral density of  $10^{-6} \text{ Hz}^{-1}$  on a white noise background, as shown in Fig. 7.

During the course of a typical spectroscopic measurement,  $V_{\text{ac}}$  is kept constant, while  $V_{\text{dc}}$  may increase to  $100V_{\text{ac}}$  or more. As a result, the corresponding ratio  $I_{\text{dc}}/I_{\text{ac}}$  may also become quite large. In order to illustrate the structure of the noise spectrum, we fix  $I_{\text{ac}} = 10$  pA (note that a fixed  $I_{\text{ac}}$  corresponds to a perfectly flat DOS as a function of energy) and plot the resulting PSD  $S_{ij}$  for different values of  $I_{\text{dc}}$  between 0 and  $100I_{\text{ac}}$ . Figure 8 shows that, as the DC bias is increased, the shot noise and  $\pm f_0$  sidebands [the  $S_{\zeta\zeta, f_0}$  term in Eqs. (16) and (17)] increase and eventually dominate the power spectrum. In Fig. 9, we illustrate how each noise power term in Eq. (17) depends on  $I_{\text{dc}}$ . We set  $I_{\text{ac}} = 10$  pA and vary  $I_{\text{dc}}$  between  $0.1I_{\text{ac}}$  and  $100I_{\text{ac}}$ , using a boxcar filter with an averaging time of 10 ms. First, near  $I_{\text{dc}} = 0$ , the noise power is determined by low frequency vibrations  $S_{\zeta\zeta, 0}$ , the preamplifier noise power  $S_{\text{aa}}$  near  $f_0$ , and the

Johnson-Nyquist current noise component of  $S_{ij}$ . Second, as  $I_{\text{dc}}$  is increased, shot noise increases  $S_{ij}$  linearly (with a slope of 1 in the log-log plot), while the  $I_{\text{dc}}^2 S_{\zeta\zeta, f_0}$  term increases quadratically (with a slope of 2 in the log-log plot) and eventually dominates the total noise power. We can expect this effect to occur in real STS measurements: as  $I_{\text{dc}}$  increases, the SNR decreases gradually below its initial level. If we would like to maintain a consistent SNR throughout a spectroscopic measurement, we can dynamically adjust the LPFs of the lock-in amplifier or averaging time to compensate for the effect of increasing  $I_{\text{dc}}$ .

As an example, we apply the boxcar filter and  $n$ th order RC filter introduced in Sec. II B on  $S_{ij}$  in Figs. 8 and 9, setting  $I_{\text{ac}} = 10$  pA

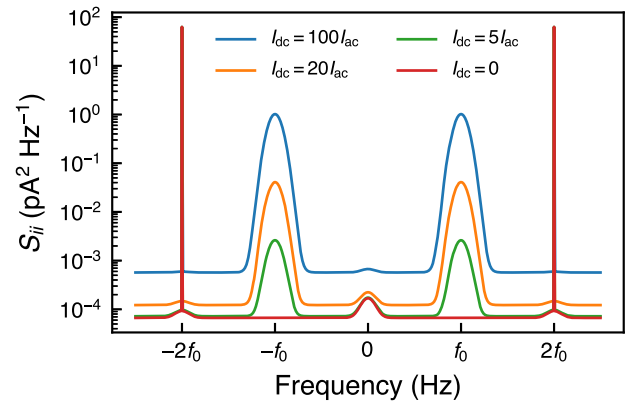


**FIG. 8.** Current PSD of the *unfiltered* demodulated signal calculated using the toy model  $S_{\zeta\zeta}$  in Fig. 7 with increasing DC current from 0 to  $100I_{\text{ac}}$ . The AC current signal power  $I_{\text{ac}}^2$  is fixed to  $100 \text{ pA}^2$ . Here,  $S_{\text{aa}} = 25 \text{ fA}^2 \text{ Hz}^{-1}$  is a typical level of a commercial preamplifier<sup>38</sup> and  $S_{ij}$  is the frequency-independent Johnson-Nyquist current noise and shot noise of the tunnel junction. See Sec. IV for complete models of  $S_{\text{aa}}$  and  $S_{ij}$ .

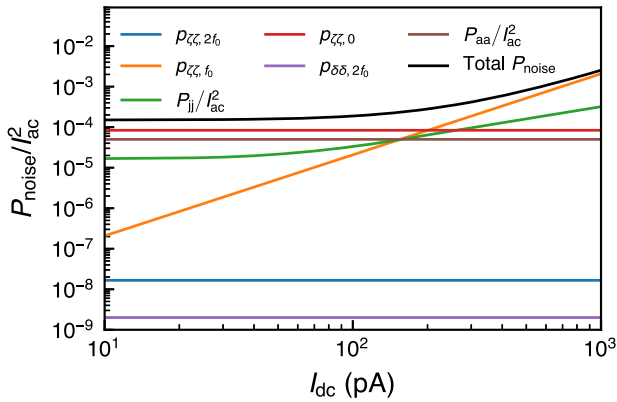


**FIG. 9.** Components of noise power calculated as a function of DC current  $I_{dc}$  from Eqs. (19) and (20) based on the toy model  $S_{\zeta\zeta}$ . Noise power is normalized by the AC current signal power  $I_{ac}^2$  of 100 pA<sup>2</sup>. A boxcar filter with a settling time of 10 ms is applied.

and  $I_{dc} = 100I_{ac}$  to obtain the noise PSD at the output of lock-in amplifier in Fig. 10. The pronounced peak of the unfiltered output is a consequence of  $S_{\zeta\zeta}$  after demodulation. Integrating each spectrum in Fig. 10 (1 Hz–100 kHz) results in a value of  $\text{SNR}^{-1}$ . For the three curves in Fig. 10, SNR values are  $-6.8$  dB for the unfiltered output,  $26.0$  dB for the boxcar filtered output, and  $28.9$  dB for the fourth-order RC filtered output. The SNR is plotted in Fig. 11(a) as a function of  $I_{dc}/I_{ac}$ , showing that different lock-in LPFs are more effective in different regimes. Alternatively, we could hold the SNR constant by adjusting the settling time of each LPF of the lock-in amplifier, as shown in Fig. 11(b). The required settling time increases with increasing ratio  $I_{dc}/I_{ac}$ . We could save valuable experiment time by reducing the settling time without sacrificing the SNR at a lower  $V_{dc}$  where normally the  $I_{dc}$  is small.

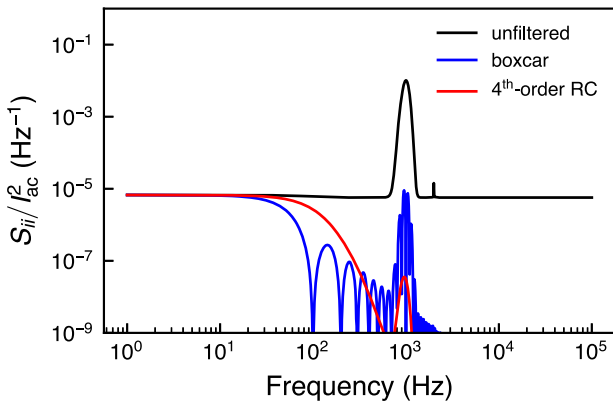


**FIG. 10.** Current noise spectral density normalized by signal power with a boxcar filter (blue), a fourth-order RC filter (red), and without a filter (black) on the output of lock-in amplifier. The response functions of the boxcar filter and the RC filter correspond to those shown in Fig. 6. Modulation frequency  $f_0 = 1000$  Hz.  $I_{dc}$  is set to  $100I_{ac}$ . The PSD spectrum is symmetric between positive and negative frequencies, so hereafter only positive sides of all the spectra are plotted.

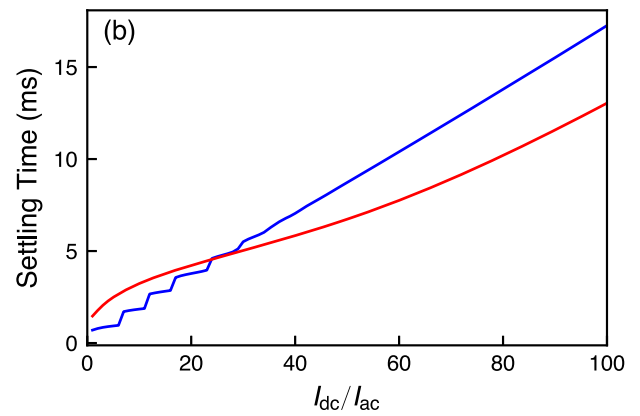
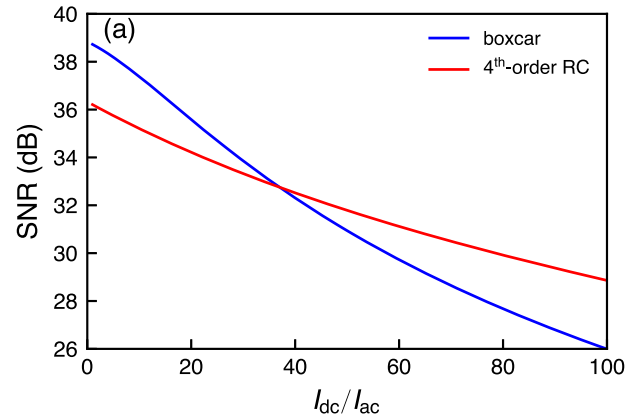


**FIG. 11.** Evaluation of SNR and optimization of settling time for the toy model. (a) SNR evaluated as a function of  $I_{dc}/I_{ac}$  with the boxcar filter and the 4th-order RC filter (as plotted in Fig. 6), with the same settling time of 10 ms. (b) Settling time estimated to maintain a constant SNR of 30 dB ( $I_{ac}^2/P_{\text{noise}} = 1000$ ). Modulation frequency  $f_0 = 1000$  Hz.

## B. Experimental determination of noise sources

The toy model is useful for demonstrating the different terms that contribute to the noise power. We can use our analysis, along with actual noise measurements from an STM instrument, to calculate the expected SNR for a range of parameters (e.g.,  $f_0$ ,  $I_{dc}$ ,  $I_{ac}$ , and  $H$ ). This calculation will allow identification of dominant noise sources, optimization of measurement parameters to maximize the SNR, and determination of design goals and benchmarks for modifying or replacing instrumentation.

In order to do so, we need to determine the actual PSD of all noise sources:  $S_{\zeta\zeta}$ ,  $S_{aa}$ , and  $S_{jj}$ , among which  $S_{jj}$  can be calculated using  $I_{dc}$  and  $V_{dc}$  [Eq. (53) in Sec. IV B 1]. To determine  $S_{aa}$  and  $S_{\zeta\zeta}$  experimentally, we set up a DC measurement (without modulating the bias voltage). Most of the terms of  $S_{ii}$  drop out and we are left with

$$S_{ii} = I_{dc}^2 S_{\zeta\zeta} + S_{aa} + S_{jj}. \quad (30)$$

To determine  $S_{aa}$ , we set  $I_{dc} = 0$  by withdrawing the tip by a few nanometers. Without tunneling current,  $S_{jj}$  vanishes [Eq. (53) in

Sec. IV B 1], only  $S_{aa}$  contributes to the measured demodulated current noise PSD  $S_{ii}$ ,

$$S_{aa} = S_{ii}(I_{dc} = 0). \quad (31)$$

As we will discuss in Sec. IV A 1, the preamplifier noise power  $S_{aa}$  may depend on the source impedance and therefore on the dynamic resistance of the junction itself. However, for simplicity, we now assume that  $S_{aa}(I_{dc} \neq 0) = S_{aa}(I_{dc} = 0)$  and we discuss later in Sec. IV A 1 when variations of  $S_{aa}$  with  $I_{dc}$  need to be taken into consideration.

To determine  $S_{\zeta\zeta}$ , we set a finite tunneling current  $I_{dc}$  with the feedback loop open (so that low-frequency  $z$  noise is not canceled). We measure the total current noise PSD  $S_{ii}$  then estimate  $S_{\zeta\zeta}$  by subtracting the previously determined  $S_{aa}$  from Eq. (31) and the calculated  $S_{jj}$  from Eq. (53),

$$S_{\zeta\zeta} = \frac{1}{I_{dc}^2} (S_{ii} - S_{aa} - S_{jj}). \quad (32)$$

Using our code,<sup>25</sup> we load two oscilloscope traces measuring current from an actual low-temperature STM, as shown in Fig. 12. We used a Pt-Ir tip and an amorphous Au foil sample at a base temperature of 4 K. We measured the preamplifier PSD  $S_{aa}$  with the tip retracted, and we measured the noise PSD  $S_{ii}$  with feedback turned off, after stabilizing at a known set point current of  $-100$  pA and a bias voltage  $V_{dc}$  of  $-0.1$  V applied to the sample. Following the method described above, in Fig. 13, we calculate the junction noise  $S_{jj}$  using Eq. (53) and estimate  $S_{\zeta\zeta}$  using Eq. (32). The reader can input his or her own data in Sec. III B of our code<sup>25</sup> and estimate  $S_{\zeta\zeta}$  for calculating the SNR.

Starting from this empirical data for the separate noise components of a DC measurement, we can simulate the process of the lock-in amplifier. Figure 14 shows the simulated *unfiltered* demodulation signal for several different values of  $I_{dc}$ . Here, we can again see the increasing noise of the sideband at modulation frequency

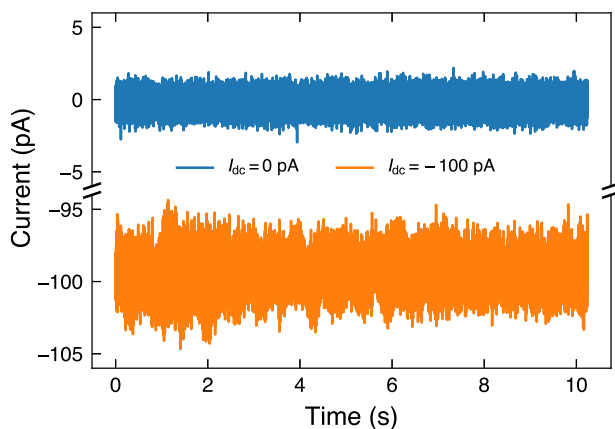


**FIG. 12.** Current fluctuation measured by an oscilloscope (built-in software module in the Nanonis BP4 controller with a sampling rate of 10 kHz) when tip is out of (blue) and in (orange) tunneling range. Feedback control was disabled during measurements.

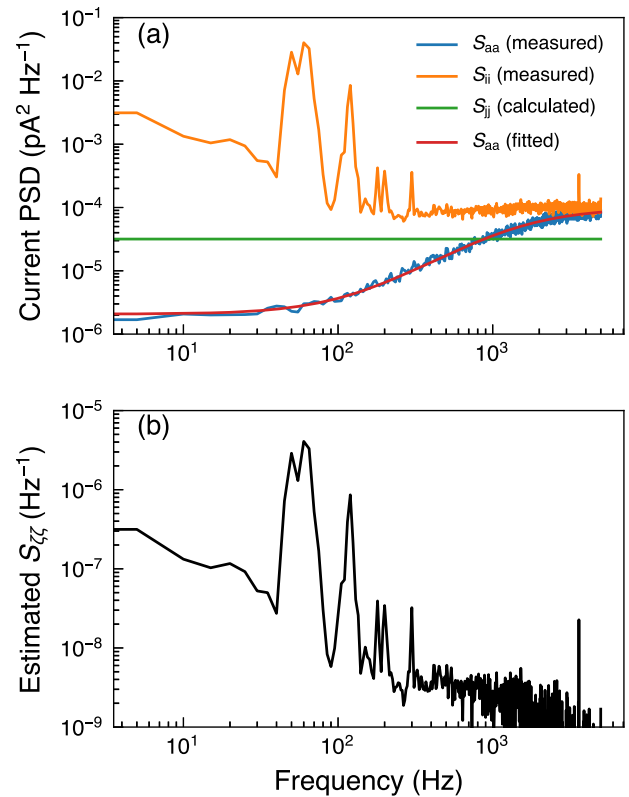


**FIG. 13.** Current PSD estimation from the two measured current time traces in Fig. 12. (a) PSD estimation was carried out using Welch's method<sup>39</sup> based on fast Fourier transform.  $S_{jj}$  was calculated based on Eq. (53) with  $|I_{dc}| = 100$  pA and  $V_{dc} = -0.1$  V,  $T_j = 4$  K.  $S_{aa}$  was fitted based on the model in Sec. IV A 1 by Eqs. (51) and (52). Fitting parameters:  $R_T = 10$  G $\Omega$ ,  $C_T = 0.8$  fF,  $C_S = 200$  pF,  $i_n = 0.8$  fA Hz<sup>-1/2</sup>, and  $v_n = 2$  nV Hz<sup>-1/2</sup>. (b) The resulting  $S_{\zeta\zeta}$  calculated by Eqs. (31) and (32) using  $S_{ii}$ ,  $S_{aa}$ , and  $S_{jj}$  in (a).

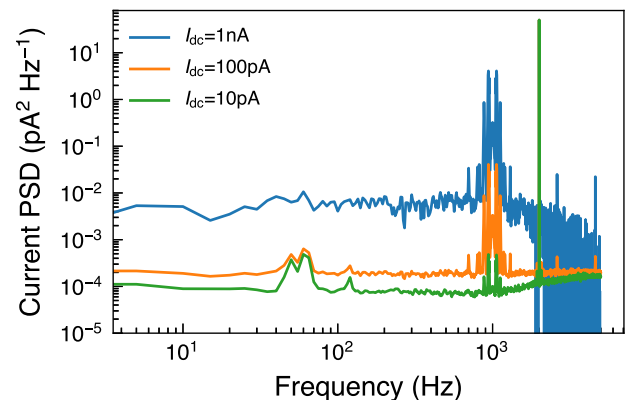


**FIG. 14.** Simulation of noise current PSD of the *unfiltered* lock-in demodulation signal according to Eq. (16), using  $S_{\zeta\zeta}$  estimated in Fig. 13(b).  $I_{ac}$  is fixed at 10 pA to illustrate how demodulated current PSD increases with  $I_{dc}$  from 10 pA to 1 nA.  $V_{dc}$  is fixed at  $-0.1$  V. Modulation frequency  $f_0 = 1000$  Hz.

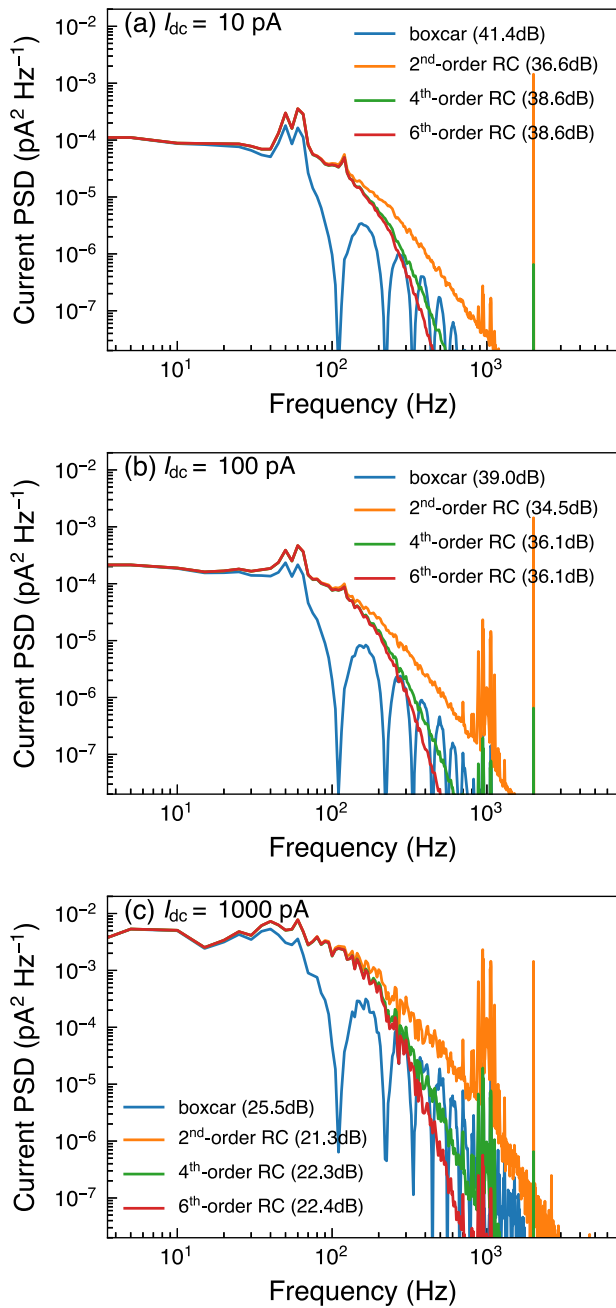


**FIG. 15.** Simulation of current PSD of the lock-in output (filtered demodulation signal).  $I_{ac}$  is fixed at 10 pA.  $V_{dc}$  is fixed at  $-0.1$  V. Modulation frequency  $f_0 = 1000$  Hz. A 2nd-order boxcar filter or a 2nd, 4th, or 6th-order RC filter with an equal settling time  $t_s = 10$  ms was applied on the unfiltered current PSD with  $I_{dc} =$  (a) 10 pA, (b) 100 pA, and (c) 1 nA in Fig. 14. SNR values are denoted after the names of the filters in the legends.

$f_0$  upon increasing  $I_{dc}$ . We also compare in Fig. 15, the choice of different LPFs on the output of the lock-in amplifier with the stipulation that the settling time (to 99.9% of the final value) is 10 ms. In Fig. 15(a), the DC bias is low, so the noise is dominated by

the low frequency  $S_{\zeta\zeta}$  spectrum. In Figs. 15(b) and 15(c), the DC current is  $10I_{ac}$  and  $100I_{ac}$ , resulting in noise spectra that are dominated by down-mixed high frequency  $S_{\zeta\zeta}$  noise, with a much lower integrated SNR. As expected, out of all filters with an equal settling

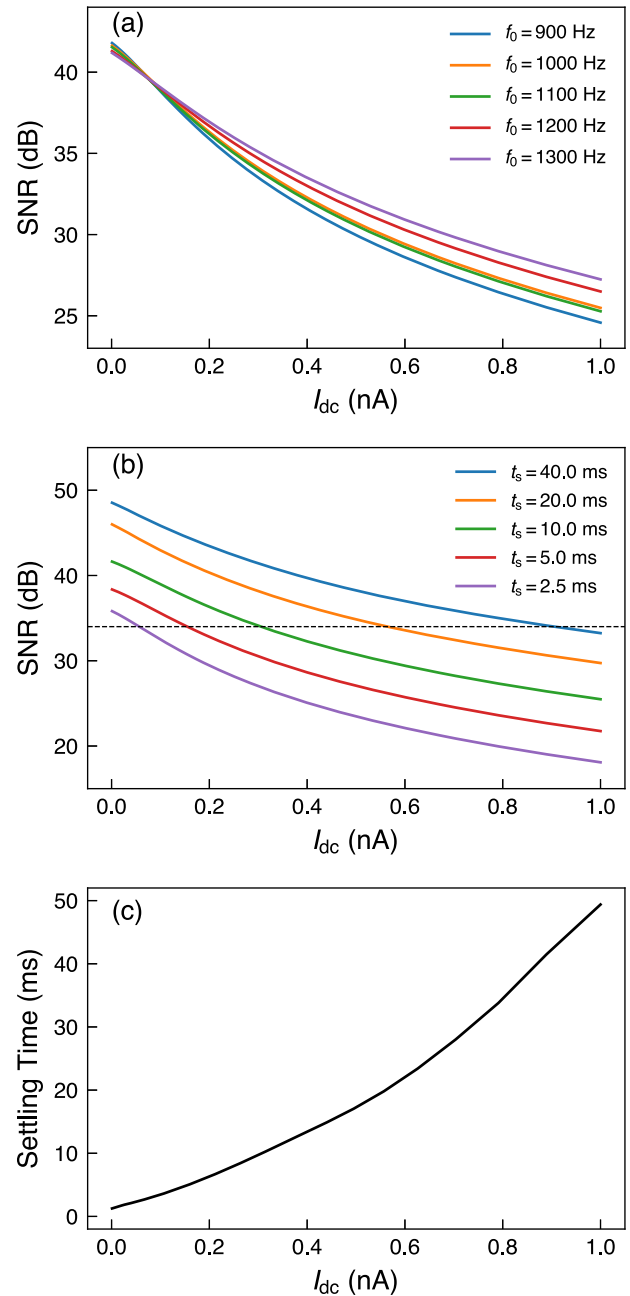


**FIG. 16.** Estimation of the SNR from Eq. (22) as a function of  $I_{dc}$ , based on  $S_{aa}$  and  $S_{\zeta\zeta}$  obtained in Fig. 13.  $I_{ac}$  is fixed at 10 pA, and a boxcar filter is used. (a) Modulation frequency  $f_0$  is tuned with fixed settling time  $t_s = 10$  ms. (b) Settling time  $t_s$  is tuned with modulation frequency fixed at  $f_0 = 1000$  Hz. (c) Required settling time of the boxcar filter as a function of  $I_{dc}$ , with fixed  $f_0 = 1000$  Hz, in order to maintain a constant SNR of 34 dB [dashed line in (b)].

time of 10 ms, the boxcar filter is most effective. The reader can carry out the same analysis with various parameters such as  $I_{dc}$ ,  $t_s$ , and  $f_0$  following the same section in our Python notebook<sup>25</sup> to predict the current PSD of the lock-in output (see Fig. 23) and calculate the corresponding SNR values.

Figure 16 shows for the example  $S_{aa}$  and  $S_{\zeta\zeta}$  how the SNR changes when we tune modulation frequency  $f_0$  and settling time  $t_s$ . A higher modulation frequency increases the SNR particularly at a high DC current. However within a single spectroscopic measurement, we cannot vary the modulation frequency due to phase change of the capacitive coupling between the tip and sample. In general, the choice of modulation frequency should be made as high as possible, without coinciding with any peak in  $S_{ii}$  or running into the roll-off frequency of the transimpedance preamplifier. We give a general step-by-step procedure for the choice of frequency in Sec. V, as there are many terms with frequency dependence in Eq. (21). On the other hand, the settling time is in principle free for the experimenter to adjust during the measurement. In Fig. 16(b), it is straightforward to adjust the settling time at different  $I_{dc}$  to maintain a constant SNR, as shown in Fig. 16(c). The reader can load his or her own data in Sec. III B of our interactive Python notebook<sup>25</sup> and then calculate the parameters [e.g.,  $t_s(V_{dc})$  for the boxcar filter at some  $f_0$ ] for an optimal dynamic LPF of the lock-in amplifier to apply. Most modern STM controllers have a programmable interface allowing users to program their own spectroscopic measurements and implement dynamic lock-in LPF parameters that can vary with  $V_{dc}$ .

#### IV. NOISE SOURCES

Section III shows how different types of noises add to affect the SNR of the measurement. We also showed how to measure some of the noise sources in a working STM, which allowed us to calculate the expected SNR under various conditions. In this section, we will take a more in-depth look at each noise source, in order to be able to perform noise diagnosis and design better instrumentation.

##### A. Transimpedance preamplifier noise $S_{aa}$

The typical tunnel junction resistance  $R_j$  is usually between  $10^5 \Omega$  and  $10^{10} \Omega$ , and the current to be measured is less than 10 nA and can be as small as 1 pA. In order to measure the small current from a high-impedance source, one generally uses a transimpedance amplifier.

###### 1. The transimpedance amplifier

We review a complete noise model for the transimpedance amplifier (TIA) circuit consisting of a single operational amplifier (abbreviated as opamp hereafter), as shown in Fig. 17. Most transimpedance amplifiers are used to read out photodiodes, which have fixed source impedance. The source capacitance  $C_s$  in an STM system is usually determined by the wiring (typically a coaxial cable of tens to hundreds of picofarad) connecting the amplifier to the tunnel junction. The source resistance  $R_s$  is dominated by the tunnel junction resistance  $R_j$ , as the cable resistance is typically less than 1 k $\Omega$ , while  $R_j$  may vary between  $10^5 \Omega$  and  $10^{10} \Omega$ .

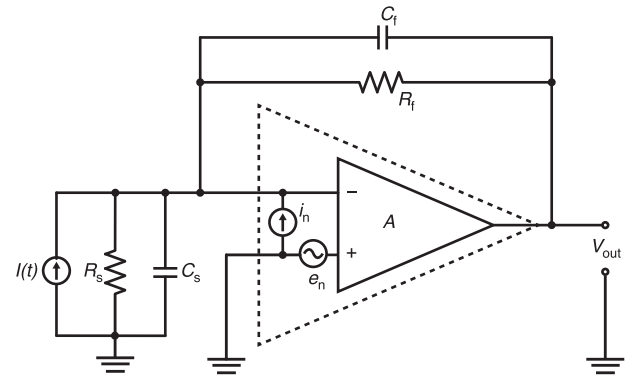


FIG. 17. Circuit diagram for noise analysis of a TIA connected to a tunnel junction. The tunnel junction is simplified by current source  $I(t)$  and junction resistance  $R_s$  in parallel with a source capacitor  $C_s$ . The dashed triangle denotes the actual opamp, while the solid triangle denotes a “noise-free” opamp.

Below are some definitions, we will use later

- $I_{in}$ : input current;
- $Z_s$ : source impedance, connecting the signal source to the inverting input;
- $Z_f$ : feedback impedance between the output and the inverting input;
- $v_n$ : input voltage noise density of the opamp;
- $i_n$ : input current noise density of the opamp;
- $A$ : open loop gain of the opamp;
- $\beta = Z_s / (Z_s + Z_f)$ : feedback factor (proportion of the output voltage that appears at the inverting input);
- $-A\beta$ : loop gain;
- $V_+$ ,  $V_-$ : the noninverting and inverting input voltages of the opamp; and
- $V_{out}$ : the output voltage of the opamp.

a. *Current gain.* The current gain can be found by solving the following two equations:

$$V_{out} = A(V_+ - V_-), \quad (33)$$

$$I_{in} = \frac{V_- - V_+}{Z_s} + \frac{V_- - V_+ - V_{out}}{Z_f}. \quad (34)$$

By rearranging terms, we find

$$V_{out} = \left( \frac{Z_f}{Z_s} + 1 \right) \frac{-V_{out}}{A} - I_{in}Z_f = -I_{in}Z_f - (A\beta)^{-1}V_{out}. \quad (35)$$

Solving for  $V_{out}$ , we find

$$V_{out} = -I_{in}Z_f \left( 1 + \frac{1}{A\beta} \right)^{-1}. \quad (36)$$

In the ideal case when the loop gain  $A\beta \gg 1$ , the current gain is  $-Z_f$ .

b. *Noise gain.* The noise gain is defined as the ratio between output voltage noise and input voltage noise. It is obtained by treating the TIA as a noninverting voltage amplifier. As before, we



write down two equations and solve for  $V_{\text{out}} = v_o$  as a function of  $V_- = v_n$ ,

$$v_o = A(v_n - V_-), \quad (37)$$

$$V_- = \beta V_{\text{out}}. \quad (38)$$

Substituting and rearranging terms, we have

$$v_o = v_n \frac{1}{\beta} \left( 1 + \frac{1}{A\beta} \right)^{-1}. \quad (39)$$

In the ideal case when the loop gain  $A\beta \gg 1$ , the noise gain is  $\beta^{-1}$ . In the opposite limit when  $A\beta \ll 1$ , the noise gain is simply  $A$  (since feedback is ineffective with such small loop gain the amplifier acts as if it were an open loop).

The open loop gain of an opamp generally takes the form<sup>40</sup>

$$A(f) = \frac{A_0}{1 + f/f_B}, \quad (40)$$

where  $f_B$  is the open-loop bandwidth (associated with another higher-frequency roll-off which will not affect this analysis) and  $A_0 \gg 1$  is the gain in the low frequency limit. The gain-bandwidth product (GBP)<sup>41</sup> of an opamp is defined as the bandwidth at unity gain  $A(f) = 1$ ,

$$f_{\text{GBP}} = A_0 f_B. \quad (41)$$

In the high frequency limit, we have  $A(f) = f_{\text{GBP}}/f$ . Therefore, the GBP is the one of the important metrics to compare the frequency performance of different opamps, and it is usually specified by manufacturers.

From Eq. (39), we know that after  $\beta^{-1}(f)$  curve intersects  $A(f)$ , the noise gain will follow  $A(f)$ . We now analyze the noise gain for  $A\beta \gg 1$  and sketch its behavior with frequency. We first write  $\beta^{-1}$  as a function of admittances instead of impedances,

$$\beta^{-1} = 1 + \frac{Z_f}{Z_s} = 1 + \frac{Z_s^{-1}}{Z_f^{-1}} = \frac{Z_s^{-1} + Z_f^{-1}}{Z_f^{-1}}. \quad (42)$$

Since admittances are additive in parallel, the numerator is just the admittance of the parallel combination of  $Z_s$  and  $Z_f$ , which we can define as  $Z_p$ , so

$$\beta^{-1} = \frac{Z_p^{-1}}{Z_f^{-1}}. \quad (43)$$

We now write the explicit form of the admittances in terms of parallel resistors and capacitors,

$$Z_f^{-1} = R_f^{-1}(2\pi j f R_f C_f + 1), \quad (44a)$$

$$Z_p^{-1} = R_p^{-1}(2\pi j f R_p C_p + 1), \quad (44b)$$

where

$$R_p^{-1} = R_s^{-1} + R_f^{-1}, \quad (45a)$$

$$C_p = C_s + C_f. \quad (45b)$$

So finally,

$$\beta^{-1} = \frac{R_f}{R_p} \frac{2\pi j f R_p C_p + 1}{2\pi j f R_f C_f + 1}. \quad (46)$$

We observe the noise gain having a zero at  $2\pi j f_p$ , where  $f_p = (2\pi R_p C_p)^{-1}$ , and a pole at  $2\pi j f_c$ , where  $f_c = (2\pi R_f C_f)^{-1}$  is the bandwidth of the TIA. At low frequency,  $\beta^{-1} \rightarrow R_f/R_p$ , while at high frequency,  $\beta^{-1} \rightarrow C_p/C_f$ .

In order for the TIA to be stable, the  $\beta^{-1}$  curve must intersect the open-loop gain curve with a relative slope of less than 40 dB/decade,<sup>43</sup> in other words, the frequency at which  $A(f) = C_p/C_f$  must be higher than  $f_c$ , or equivalently

$$f_{\text{GBP}} > \frac{C_p}{C_f} f_c = \left( \frac{C_s}{C_f} + 1 \right) f_c \approx 2\pi R_f C_s f_c^2, \quad (47)$$

when  $C_f \ll C_s$ . The source capacitance  $C_s$  is determined by the sum of TIA input capacitance and the capacitance of the wiring connecting the tunnel junction to the TIA. The typical cable for a low-temperature STM has a capacitance of 50–300 pF. For example with  $R_f = 1 \text{ G}\Omega$ ,  $C_s = 200 \text{ pF}$ , a stable TIA with a bandwidth of 4 kHz would require a minimum GBP of 20 MHz, but increasing  $C_s$  to 1 nF would require GBP to be above 100 MHz.

In Fig. 18, we calculate the current gain, loop gain, and noise gain for a TIA using the parameters for a commercially available opamp with a GBP of 22 MHz, requiring a gain of 1 GV/A and a bandwidth of 4 kHz, and assuming a source capacitance of 200 pF. As we choose a source resistance that is much higher than the feedback resistance, the resulting noise gain of  $R_f/R_p$  approaches 1 at low-frequency limit. At high-frequency limit, the noise gain reaches  $C_p/C_s$ , then rolls off due to finite open-loop gain. Note that the  $C_f$  required to obtain a bandwidth of 4 kHz is as small as 0.04 pF. It is smaller than the typical parasitic capacitance for even the smallest surface mount resistors (usually around 0.15 pF), so it requires the use of multiple resistors in series with careful layout, or a more complex feedback network.<sup>44</sup>

We note that the source impedance influences the noise gain in Eq. (46). In Fig. 19(a), we plot the noise gain while reducing the source resistance from  $10^{10} \Omega$  to  $10^5 \Omega$ , which covers the range of most STM tunnel junction resistances. Conversely, we plot the noise gain with a fixed source resistance  $R_s = 10^{10} \Omega$ , but a varying source capacitance from 1 pF to 10 nF in Fig. 19(b). Note the noise gain peaks at 1nF and above, indicating an unstable TIA. It occurs because the GBP of 22 MHz we used is insufficient according to Eq. (47).

## 2. Input-referred noise

The output voltage noise density is determined by three uncorrelated noise generators, which must be summed in quadrature,

1. The input current noise  $i_n$  is amplified by the current gain,

$$v_{o(i)} = -i_n Z_f \left( 1 + \frac{1}{A\beta} \right)^{-1}. \quad (48)$$

2. The input voltage noise  $v_n$  is amplified by the noise gain,

$$v_{o(e)} = \frac{v_n}{\beta} \left( 1 + \frac{1}{A\beta} \right)^{-1}. \quad (49)$$

3. The Johnson-Nyquist current noise of the feedback resistor  $R_f$  appears at the output without gain,

$$v_{o(T)} = \sqrt{2k_B T R_f}. \quad (50)$$

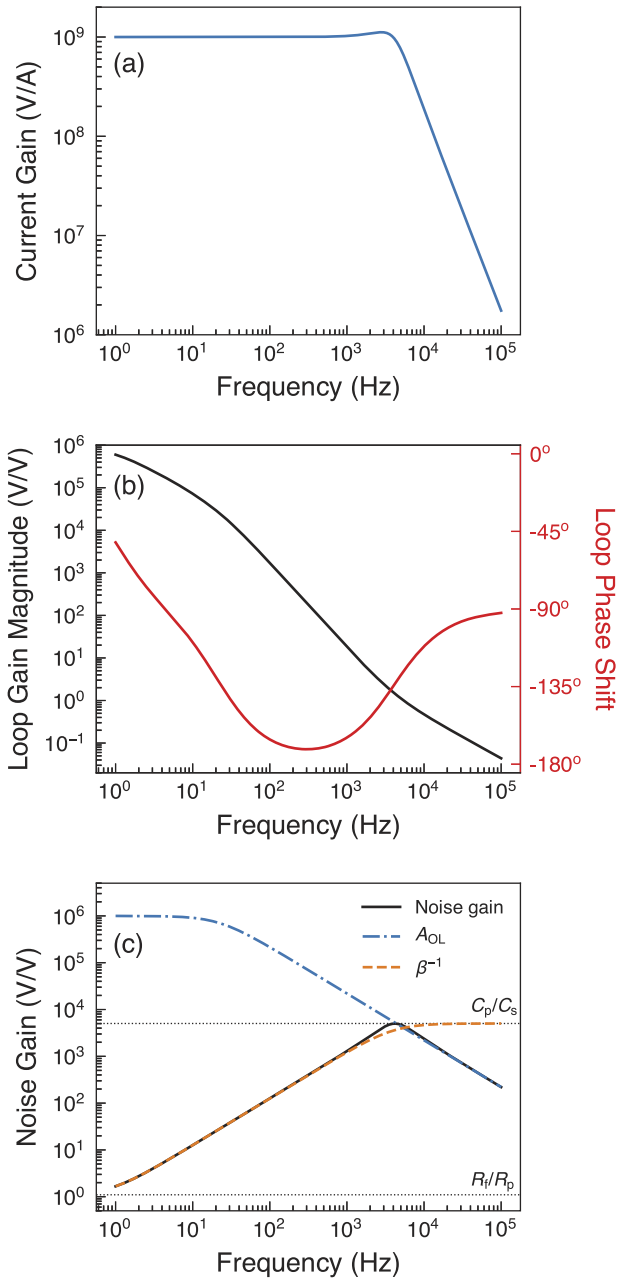


**FIG. 18.** (a) Current gain, (b) loop gain, and (c) noise gain calculated as a function of frequency for an actual TIA based on a commercially available opamp.<sup>42</sup> Parameters:  $R_f = 1 \text{ G}\Omega$ ,  $C_f = 40 \text{ fF}$ ,  $R_s = 10 \text{ G}\Omega$ ,  $C_s = 200 \text{ pF}$ ,  $f_{\text{GBP}} = 22 \text{ MHz}$ , and  $A_0 = 10^6 \text{ V/V}$ . The resulting current gain is  $10^9 \text{ V/A}$  up to 4 kHz. In (b), a phase margin (phase shift at unity loop gain) of  $54^\circ$  is obtained and the phase shift does not cross  $180^\circ$  up to 100 kHz.

The total output voltage noise PSD is

$$\begin{aligned} v_o^2 &= v_{o(i)}^2 + v_{o(e)}^2 + v_{o(T)}^2 \\ &= 2k_B TR_f + \left( i_n^2 |Z_f|^2 + \frac{v_n^2}{\beta^2} \right) \left( 1 + \frac{1}{A\beta} \right)^{-1}. \end{aligned} \quad (51)$$

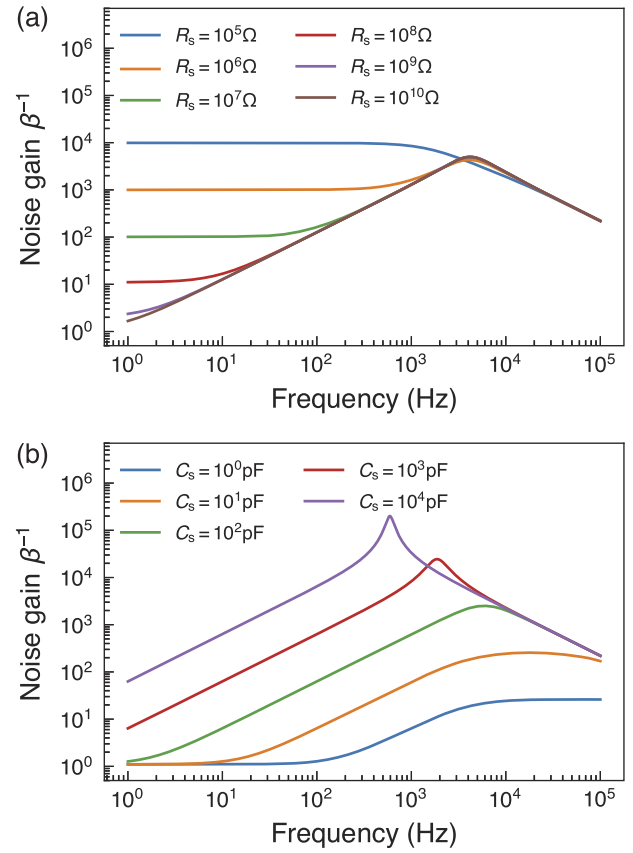


**FIG. 19.** Noise gain calculated as a function of frequency with different source impedance. (a) Source capacitance  $C_s$  is fixed at 200 pF and (b) source resistance  $R_s$  is fixed at 10 G $\Omega$ . Other parameters are the same:  $R_f = 1 \text{ G}\Omega$ ,  $C_f = 40 \text{ fF}$ ,  $f_{\text{GBP}} = 22 \text{ MHz}$ , and  $A_0 = 10^6 \text{ V/V}$ .

Equation (51) gives us an expression for the input-referred preamplifier current noise PSD  $S_{aa}$ , which we defined in Sec. II,

$$S_{aa} = v_o^2 / R_f^2. \quad (52)$$

It is important to note that while this expression depends on the source resistance (that appears in  $\beta$ ), it does *not* include noise generated by the source (the tunnel junction). The source resistance appears as a factor in current gain, noise gain, and loop gain in Eqs. (48)–(52). We include all noise generated by the source resistance in  $S_{jj}$  in Sec. IV B 1.

We calculate the input-referred current noise PSD  $S_{aa}$  for two possible TIA configurations in Fig. 20, assuming  $R_s \gg R_f$ , showing the contribution of each of the three noise generators along with the total input noise. We can see that the low-frequency noise is dominated by the Johnson-Nyquist current noise and/or input current noise, while high-frequency noise is dominated by the input voltage noise. The reader can plug in the parameters for a desired opamp to be used for a TIA in our code<sup>25</sup> and calculate the resulting  $S_{aa}$ .

As we mentioned in Sec. III B,  $S_{aa}$  may vary with  $I_{dc}$  when the bias  $V_{dc}$  is kept constant. In other words, the junction resistance can

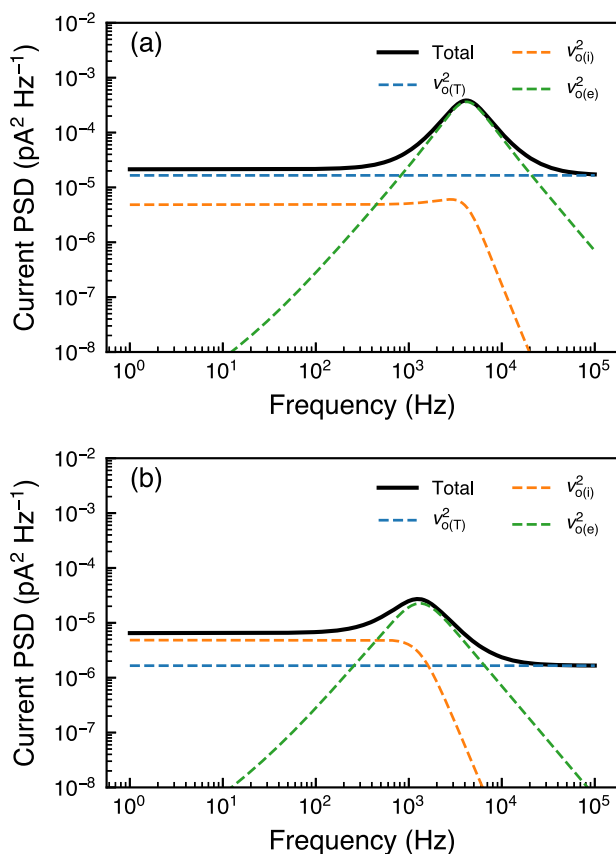


**FIG. 20.** Input-referred noise current PSD of two TIA configurations based on a commercially available opamp with  $f_{\text{GBP}} = 22$  MHz and  $A_0 = 10^6$  V/V.<sup>42</sup> (a) The TIA with a gain of 1 GV/A and a bandwidth of 4 kHz. Parameters:  $R_f = 1$  G $\Omega$ ,  $C_f = 40$  fF,  $R_s = 100$  G $\Omega$ , and  $C_s = 200$  pF. (b) The TIA with a gain of 10 GV/A and a bandwidth of 1 kHz. Parameters:  $R_f = 10$  G $\Omega$ ,  $C_f = 15.9$  fF,  $R_s = 100$  G $\Omega$ , and  $C_s = 200$  pF. The integrated rms current noise is (a) 2.03 pA and (b) 0.48 pA.

vary by orders of magnitude, which in turn may affect  $S_{aa}$  at low frequency. We use the example of TIA shown in Fig. 20(a) and decrease the source resistance from 100 M $\Omega$  to 0.1 M $\Omega$ . Figure 21 shows that the low frequency noise increased by order of magnitudes when the source resistance is below 1 M $\Omega$ .

### 3. Comparison between cryogenic and room-temperature preamplifiers

From Eq. (51) and Fig. 20, we know that input voltage noise  $v_n$ , amplified by noise gain  $\beta^{-1}$ , dominates to  $S_{aa}$  at high frequencies. The cause is the noise gain reaching a constant  $1 + C_s/C_f$  at high frequencies before roll-off by  $A(f)$ . In the conventional set up of an STM where the preamplifier sits outside ultrahigh vacuum (UHV) and cryogenic environment, it is difficult to reduce the noise gain because of the large wiring capacitance  $C_s$ . To minimize the input voltage noise, one can essentially choose a low noise opamp (which may have a high input capacitance) or reduce the ratio of  $C_s/C_f$ . While increasing  $C_f$  reduces the bandwidth of the TIA, one

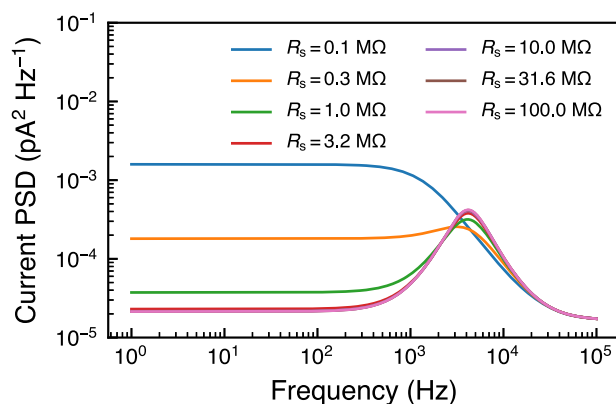


**FIG. 21.** Input-referred noise current PSD with different source resistances. The TIA configuration is the same with Fig. 20(a), except that the input voltage noise  $v_n$  is a frequency-independent constant at  $4$  nV Hz<sup>-1/2</sup>.

can decrease  $C_s$  by shortening the coaxial cable to a few centimeters, which may bring the preamplifier into UHV, cryogenic environment, and physically close to the tunnel junction. It also lowers the Johnson-Nyquist voltage noise  $v_{o(T)}$  of the feedback resistor by a factor of 8.7 from 300 K to 4 K.

Cryogenic (first-stage) preamplifiers have been developed and improved over decades. The central component of the opamps is the transistor. We list four types of field effect transistors (FETs) that are compatible with the cryogenic environment, namely, Si-based junction FETs (Si-JFETs),<sup>45,46</sup> Si-based metal-oxide-semiconductor FET (Si-MOSFETs),<sup>47-50</sup> GaAs-based metal-semiconductor FET (GaAs-MESFETs),<sup>51-54</sup> and GaAs-based metal-oxide-semiconductor FET (GaAs-MOSFETs).<sup>55-58</sup> We describe the advantages and disadvantages of different types of FETs in the following:

1. Si-JFETs have relatively low flicker noise, but they can only work above 40 K due to charge freeze-out below 40 K.<sup>45,46</sup> In other words, JFETs have to be placed away from the 4 K bath, which contradicts our intention of reducing cable length. In addition, JFETs' intrinsic input capacitance is relatively high, usually a few 10 pF.
2. Si-MOSFETs could be used below 40 K without charge freeze-out basically by transmitting more power to the conduction channel via overrated supply voltages.<sup>47</sup> Charge trapping is more pronounced at low temperatures, which increases flicker noise by one order of magnitude from 300 K to 4 K.<sup>49</sup>
3. GaAs-MESFETs work based on two-dimensional electron gas with high mobility and do not suffer from charge freeze-out at the lowest temperature. High electron mobility transistors (HEMT) are even made for preamplifiers running at megahertz frequency with the aid of impedance matching.<sup>54,59,60</sup> However, they require extreme care in handling and delicate matching of units to reduce bias shift<sup>53</sup> and should be cooled down properly to prevent telegraph noise. Intrinsic noise at 4 K measured after second stage voltage amplifier is not yet lower than room temperature preamplifiers with the same gain.<sup>53</sup>
4. GaAs-MOSFETs would be the best candidate for cryogenic signal readout with their low noise and high carrier mobility but

have yet to be improved especially the quality of their oxide layers.<sup>58</sup>

In principle, one can balance between noise and bandwidth and design cryogenic preamplifiers based on one of the above four types of FETs to lower the input-referred current noise and increase the bandwidth of the current signal for high-speed spectroscopic measurements.<sup>60,61</sup>

## B. Tunnel junction noise $S_{jj}$

Here, we discuss noise generated in the tunnel junction, from three main sources: the Johnson-Nyquist current noise and shot noise of the junction current (denoted by  $i_j$ ), bias voltage noise (denoted by  $v_{n,DAC}$ ), and electromagnetic interference (EMI) voltage noise (denoted by  $v_{n,EMI}$ ), as shown in Fig. 4.

### 1. Johnson-Nyquist noise and shot noise

In general, current fluctuations in the tunnel junction depend on the  $I(V)$  characteristics of the junction, as discussed in detail in Ref. 62. Practically, all STS measurements are done in the extreme low frequency limit ( $f \ll eV/h$ ,  $f \ll k_B T/h$ ) because  $k_B T/h = 0.21$  GHz at  $T = 10$  mK and  $e \times 1 \mu V/h = 0.24$  GHz at  $V = 1 \mu V$ . In this low-frequency limit, the junction noise PSD is

$$S_{jj} = eI \coth\left(\frac{eV}{2k_B T_j}\right), \quad (53)$$

which describes shot noise in the high-voltage limit ( $|eV| \gg k_B T$ ),<sup>63</sup>

$$S_{jj} = e|I|, \quad (54)$$

and the Johnson-Nyquist current noise in the low-voltage limit ( $|eV| \ll k_B T$ ),

$$S_{jj} = 2k_B T_j \frac{I}{V} = \frac{2k_B T_j}{R_j}, \quad (55)$$

where  $R_j$  is the junction resistance assuming a linear  $I(V)$  characteristic.

Under some conditions, the junction shot noise and the Johnson-Nyquist current noise may dominate the noise from the TIA.

- Shot noise: when  $V_{out} = I_{dc} R_f > 2k_B T_f/e$ , the junction shot noise exceeds the Johnson-Nyquist current noise of the feedback resistor. At  $T_f = 300$  K, junction shot noise dominates when the TIA output voltage exceeds 50 mV (independent of feedback resistor value).
- Johnson-Nyquist current noise: if  $T_j = 300$  K and  $R_j < R_f$ , the Johnson-Nyquist current noise of the junction will exceed the Johnson-Nyquist current noise of the feedback resistor. In general, we can expect the junction to dominate when  $R_j/T_j < R_f/T_f$ .

Figure 22 exemplifies the dominance of  $S_{jj}$  for a room-temperature TIA with gain 1 GV/A, and various tunnel junction resistances  $R_j$  and temperatures  $T_j$ . The reader can evaluate  $S_{jj}$  using our code<sup>25</sup> in various experimental conditions.  $S_{jj}$  can be considerably higher than  $S_{aa}$  at higher bias voltages (assuming the feedback resistor noise dominates  $S_{aa}$ ). As a result, the measured  $I(V)$  and  $g(V)$  fluctuate substantially at higher  $V_{dc}$ , a common problem in

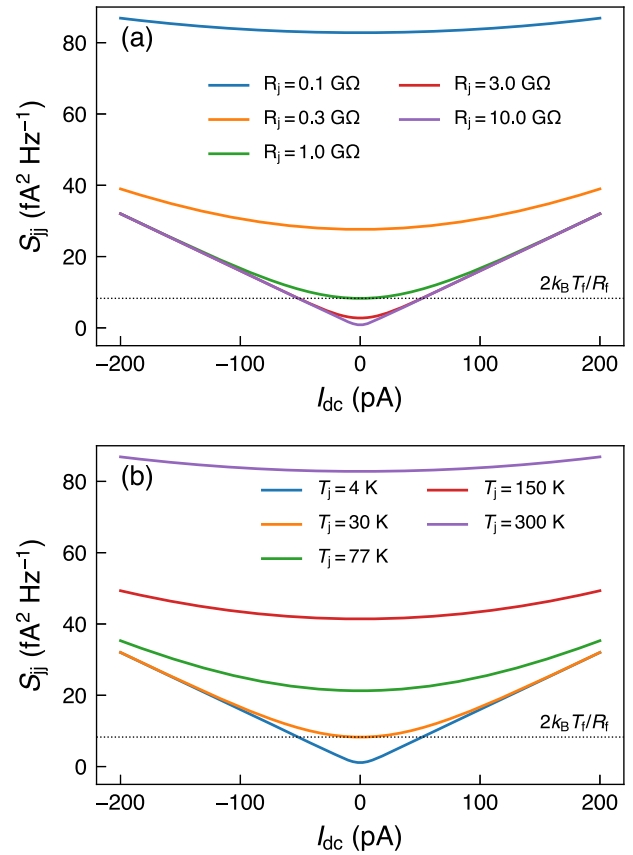


**FIG. 22.** Junction noise current PSD calculated from Eq. (53) as a function of  $I_{dc}$  (a) with different  $R_j$  (equivalent to source resistance  $R_s$ ) and (b) at different junction temperature  $T_j$ . (a)  $T_j$  is fixed at 300 K and (b)  $R_j$  is fixed at  $100 \text{ M}\Omega$ . The dotted lines in both figures show the effective Johnson-Nyquist current noise ( $2k_B T_f/R_f$ ) from the feedback resistor  $R_f = 1 \text{ G}\Omega$  of the TIA with  $T_f = 300$  K as a reference.

spectroscopic measurements using a fixed LPF for the lock-in amplifier, as shown in Fig. 3(b). For this reason, it is intuitive to apply a dynamic LPF in the lock-in amplifier, adjusting noise bandwidth for each point of bias voltage. The advantage of a dynamic LPF is twofold: first, at low  $V_{dc}$ , the LPF noise bandwidth can be larger so we save time; second, a constant SNR as a function of bias voltage can be achieved.

Note that throughout previous discussions we have implicitly assumed equal temperature  $T_j$  for the tip and sample. Recently, it was demonstrated by quantum point contact experiments<sup>64</sup> that a temperature difference across the tunnel junction could introduce an additional term  $\Delta S_{jj}(\Delta T)$  to the junction noise in Eq. (53),

$$\Delta S_{jj}(\Delta T) = \frac{1}{4} \left( \frac{\pi^2}{9} - \frac{2}{3} \right) \left( \frac{\Delta T}{\bar{T}} \right)^2 2k_B \bar{T}/R_j, \quad (56)$$

where  $2k_B \bar{T}/R_j$  is the average Johnson-Nyquist current noise of the tunnel junction,  $\bar{T}$  is the arithmetic average of tip temperature  $T_{tip}$  and sample temperature  $T_{sample}$ , and  $\Delta T$  is the absolute difference between  $T_{tip}$  and  $T_{sample}$ . This excess term  $\Delta S_{jj}(\Delta T)$  could reach 15%

of the average junction Johnson-Nyquist current noise if the temperature of one side of the junction is 4 times the temperature of the other side (e.g.,  $T_{\text{sample}} = 1$  K but  $T_{\text{tip}} = 4$  K). Therefore, in STM design, one should consider thermal anchoring, not only for the sample but also for the tip, to minimize the temperature difference between them.

## 2. Bias voltage

Bias voltage noise contributes to junction noise as well, in the form of  $v_{n,\text{DAC}}/R_j$ , as shown in Fig. 4. For a typical 20-bit digital-to-analog converter (DAC) with a range of  $\pm 10$  V and speed up to  $10^6$  samples/s, the output voltage has a noise floor of around  $20$  nV  $\text{Hz}^{-1/2}$ . It is comparable to the Johnson-Nyquist voltage noise of a tunnel junction of  $2$  M $\Omega$  at  $4$  K. For the typical working range of STM, the voltage noise of DACs for the bias voltage is thus negligible, but we will see in Sec. IV C 1 that  $v_{n,\text{DAC}}$  enters  $S_{\zeta\zeta}$  after amplification.

## 3. Electromagnetic interference

We include electromagnetic interference (EMI) in the junction current noise, though technically the electromagnetic noise pick-up could occur not only at the tunnel junction but also in the wiring. At high frequency, EMI is known as radio-frequency noise, coupled via radiation to the whole STM circuitry. If the STM unit is well shielded, then the interference mostly occurs in the wires and cables running from the controllers to the STM. At low frequency, EMI exhibits as ground-loop induction, usually at the line frequency and its harmonics. The noise sources, however, are not intrinsic. Eliminating EMI is a topic extensively discussed in the literature,<sup>65–67</sup> and it should be carried out prior to STM noise characterization.

## C. Tip-sample distance modulation noise $S_{\zeta\zeta}$

Tip-sample distance fluctuation introduces noise that scales with the signal (both AC and DC); therefore, the power of dimensionless quantity  $\zeta$  appears in the SNR of Eq. (21). In this section, we discuss three factors that influence  $S_{\zeta\zeta}$ : piezo control voltage noise, fluctuation of apparent barrier height, and mechanical vibration.

### 1. Piezo control voltage noise

In STM, we actuate the tip by applying a high voltage across the scanner piezos. A standard sample with a known lattice (e.g., Si or Au crystal) is used to calibrate the piezo motion with respect to applied voltage. The calibration factor is usually on the order of a few nanometers per volt. On the other hand, in the feedback loop, an error signal between instantaneous value and set point of the current is generated, and it adds to the  $z$  piezo voltage to move the tip accordingly to maintain a constant current. The error signal is low voltage (an output of a DAC) and amplified by a high voltage amplifier (HVA). Additionally, the DAC output noise, which accompanies the error signal, is amplified with the same gain. The total control voltage noise is the sum of the amplified noise and the output voltage noise of the HVA itself (even when the feedback loop is open), as shown in Fig. 4. As a consequence, one can estimate tip-sample distance modulation due to noise from piezo control voltage. For instance, frequency-independent noise with an amplitude spectral density of  $1$   $\mu\text{V Hz}^{-1/2}$  multiplied by a  $1$  nm/V calibration factor

results in  $1$  fm  $\text{Hz}^{-1/2}$  in the  $z$  direction. After the conversion, one can compare the piezo control voltage noise with the mechanical vibration.

When spectroscopic measurements are being performed, the feedback loop is open in order to have a constant tip-sample distance. In this case, any fluctuation in HVA outputs (not only  $z$  but also  $x$  and  $y$ ) would cause fluctuation in the tip-sample distance. One can add switchable low pass filters (with a cutoff frequency on the order of  $\sim 0.5$  Hz) after the HVA outputs<sup>68</sup> and activate the LPFs for the HVA outputs to attenuate AC noise from the DACs and the HVA (only during spectroscopy, as the feedback control signal would also be attenuated in the closed feedback loop). Furthermore, as DC drift cannot be filtered out by the LPFs of the HVA outputs, care must be taken to avoid substantial temperature changes in the HVAs, since input offset voltage could drift  $\sim 0.05$  mV/ $^\circ\text{C}$ , which yields  $\sim 1$  pm/ $^\circ\text{C}$  at a gain of 20. This temperature change is concerning because the HVAs draw considerable power ( $\sim 5$  W per opamp), so sufficient air cooling must be implemented for the HVAs.

### 2. Apparent barrier height

In Eq. (6), we treat  $\kappa$  as a constant, or at least insensitive to change in bias voltage or tip-sample distance, which is generally the case. Here, we need to emphasize that in some situations  $\kappa$  may vary spatially<sup>69</sup> or as a function of applied bias voltage,<sup>8</sup> which effectively introduces fluctuation in current. For a rectangular tunnel barrier,<sup>70,71</sup>

$$\kappa = \frac{2}{\hbar} \sqrt{2m\phi_a}, \quad (57)$$

where  $\phi_a$  is the apparent barrier height, usually considered as a constant yielding to the average work function of the tip and sample. However, experiments<sup>72</sup> show that close to crystal step edges, due to dipole moment build-up (Smoluchowski effect<sup>73</sup>),  $\phi_a$  varies with applied voltage up to  $\sim 15\%$ /V in the intermediate bias range. Furthermore, local chemical potential on the sample surface may fluctuate spatially and result in variation of  $\kappa$  by as much as 60%.<sup>69</sup> Compensation methods based on local barrier height measurements<sup>74</sup> are needed for such samples before performing spectroscopic measurements.

### 3. Mechanical vibration

The other part in the dimensionless quantity  $\zeta$  is the fluctuation in tip-sample distance  $z_n(t)$ . Since  $\kappa$  is typically  $2$   $\text{\AA}^{-1}$ ,  $z_n$  exceeding  $1$  pm results in 2% variation in the current signal. The environmental noise, mainly mechanical vibration and acoustic noise, could easily excite  $z_n$  over  $1$  pm if the tip-sample junction is lightly coupled to the laboratory environment. To minimize the acoustic noise, one can move all the sound sources out and apply sound absorbing materials on the walls of the lab room. On the other hand, mechanical vibration is always a major concern in system design of all STMs. Vibration transfer is quantified by the overall structure transfer function  $K$  in Fig. 4, which is approximately<sup>35</sup>

$$K(f) \approx \left( \frac{f_1}{f_s} \right)^2, \quad (58)$$

where  $f_1$  and  $f_s$  are natural frequencies of the isolators and STM, respectively. It is immediately clear that one should increase  $f_s$  and decrease  $f_1$  to minimize vibration noise. First, multistage isolators



including suspension springs, pneumatic systems, and eddy-current dampers are commonly used to decrease  $f_1$  but limited down to  $\sim 1$  Hz; second, it is important to improve the stiffness-to-weight ratio of the STM unit in order to increase  $f_5$ ; and third, an alternate approach is feasible to measure the transfer function and apply real-time (synchronized) vibration cancellation to the current signal. Since it is beyond the scope of this article, here, we direct the readers to one good example of each method, in Refs. 53, 59, and 75, respectively.

## V. CONCLUSION

In this article, we give an explicit expression for the SNR in scanning tunneling spectroscopy, a flowchart to decompose the various noise sources and their relations, and a computer code<sup>35</sup> to estimate each noise source and to predict the SNR with different experimental parameters. We provide an example of noise in an actual STM, give suggestions for low-pass filters of the lock-in amplifier to enhance the SNR, and offer methods to keep the SNR constant during a spectroscopic measurement. We discuss in detail the noise sources from the transimpedance preamplifier, the tunnel junction, and the tip-sample distance fluctuation. Through iterations of eliminating or suppressing the noisiest source, one can achieve a stable low noise condition in scanning tunneling spectroscopic measurements.

As pointed out in Sec. I, time is the major limiting factor in QPI imaging with atomic resolution. We suggest an algorithm to optimize the SNR in single-point spectroscopy before launching a lengthy QPI measurement that lasts a few days.

1. Measure  $S_{aa}$  by withdrawing the tip by a few nanometers [Figs. 12 and 13(a)] and compare it with the model  $S_{aa}$  in Sec. IV A 1 or noise specification curves if a commercial preamplifier is used. Suppress all extra noise peaks (normally at the line frequency and its harmonics) by inspecting EMI introduced to the system.
2. Measure  $S_{ii}$  in a DC measurement [Figs. 12 and 13(a)] at the desired setup bias voltage and current set point with feedback control disabled, and extract  $S_{\zeta\zeta}$  according to Eq. (32) [Fig. 13(b)].
3. Find corner frequency  $f_F$  of flicker noise (Fig. 1) and compare flicker noise power  $P_F$  with preamplifier noise  $P_{amp}$  using Eq. (4). If  $P_F > P_{amp}$ , the lock-in method should be applied for STS measurements; otherwise, the DC method should be used.
4. Inspect noise peaks in  $S_{\zeta\zeta}$  and suppress the corresponding environment vibration noise sources if possible.
5. Pick an initial modulation frequency  $f_0$  that has a low noise spectral density in  $S_{ii}$ . Note that  $f_0$  cannot be larger than  $f_{amp}$ .
6. Perform a single STS measurement for converting  $V_{dc}$  to  $I_{dc}$  [Fig. 3(a)] and obtaining the ratio of  $I_{dc}/I_{ac}$  as a function of  $V_{dc}$ .
7. Calculate the SNR as a function of  $V_{dc}$  with Eq. (22), using the relation between  $I_{dc}/I_{ac}$  and  $V_{dc}$  obtained in the previous step.
8. Calculate the SNR as a function of modulation frequency  $f_0$  [Fig. 16(a)] and change  $f_0$  to a frequency that has an overall higher SNR in the measured range of  $I_{dc}$ . Note that both  $f_0$  and  $2f_0$  should be away from frequencies of existing

noise peaks to avoid considerable cross-correlation terms in Eq. (12).

9. Calculate the filter parameters for the lock-in amplifier, such as settling time of boxcar or RC filter as a function of  $V_{dc}$  to keep the SNR constant (Fig. 11).
10. Apply the dynamic low-pass filter from the previous step to the lock-in amplifier and perform another STS measurement to check the SNR [Fig. 3(a)]. Iterate steps 5–9 until a constant SNR is achieved.

Once the SNR is optimized in single-point spectroscopic measurements, one typically saves time at low bias voltages, where the SNR is generally higher than the SNR at higher bias voltages for a static LPF of the lock-in amplifier (Fig. 16). We also recommend testing the dynamic LPF setting for the lock-in amplifier on a few spatial locations. By improving noise conditions and dynamically optimizing the LPF parameters of the lock-in amplifier, efficiency can be substantially increased in STS measurements and QPI imaging.

## ACKNOWLEDGMENTS

This work was supported by the National Science Foundation under Grant No. DMR-1231319 (STC Center for Integrated Quantum Materials).

## NOMENCLATURE

### Acronyms

ARPES	angle-resolved photoemission spectroscopy
DAC	digital-to-analog converter
DOS	density of states
ENBW	equivalent noise bandwidth
EMI	electromagnetic interference
FET	field-effect transistor
FT	Fourier transform
GBP	gain-bandwidth product
HVA	high-voltage amplifier
LPF	low-pass filter
PSD	power spectral density
QPI	quasiparticle interference
rms	root-mean-square
SNR	signal-to-noise ratio
STM	scanning tunneling microscopy
STS	scanning tunneling spectroscopy
TIA	transimpedance amplifier
UHV	ultrahigh vacuum

### Symbols

$g$	differential conductance ( $A V^{-1}$ )
$I$	current (A)
$i$	current noise (A)
$\mathbf{r}$	spatial location (m, Å)
$V$	voltage (V)
$v$	voltage noise (V)
$\mathbf{q}$	momentum transfer ( $m^{-1}$ , Å $^{-1}$ )
$\mathbf{k}$	momentum ( $m^{-1}$ , Å $^{-1}$ )
$P$	power of the current ( $A^2$ )
$t$	time (s)

$T$	temperature (K)
$f$	frequency (Hz)
$\kappa$	current decay constant ( $\text{m}^{-1}$ , $\text{\AA}^{-1}$ )
$z$	tip-sample distance (m, $\text{\AA}^{-1}$ )
$\zeta$	dimensionless fluctuation factor [Eq. (8c)] (1)
$\delta$	dirac delta function
$S$	power spectral density
$j$	unit imaginary number
$e$	elementary charge (C)
$R$	resistance ( $\Omega$ )
$H$	frequency response function
$p$	specific current power (1)
$B_N$	equivalent noise bandwidth (Hz)
$h$	impulse response function in the time domain
$y$	step response function in the time domain
$C$	capacitance (F)
$Z$	impedance ( $\text{V A}^{-1}$ )
$A$	open loop gain (1)
$\beta$	feedback factor
$k_B$	Boltzmann constant ( $\text{J K}^{-1}$ , $\text{eV K}^{-1}$ )

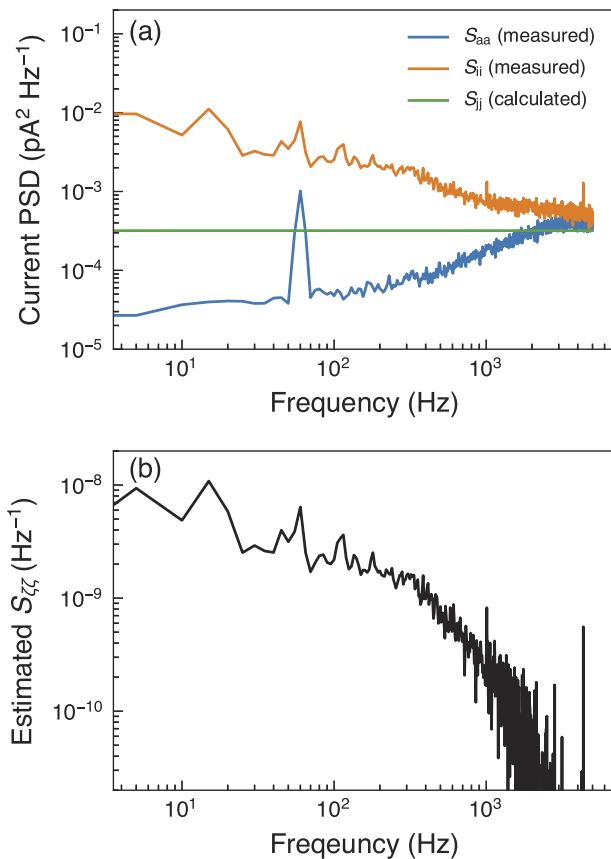


**FIG. 23.** (a) Estimated PSDs of the tip out of (blue) and in (orange) tunneling range. The measurements (current traces not shown) were carried out with a PtIr tip and CeBi sample at 4 K with feedback control disabled. Setup conditions:  $V_{dc} = 0.4$  V and  $I_{dc} = 1$  nA. The corresponding  $S_{ij}$  was calculated based on Eq. (53). (b)  $S_{zz}$  calculated by Eqs. (31) and (32) using  $S_{ii}$ ,  $S_{aa}$ , and  $S_{ij}$  in (a).

$\phi_a$	apparent barrier height (J, eV)
$K$	mechanical transfer function

## APPENDIX: OMISSION OF THE CROSS-CORRELATION TERMS IN THE NOISE POWER SPECTRUM DENSITY

We derive Eq. (14) in Sec. II A from Eq. (12) with the approximation that cross-correlation terms between the same function with different frequency shifts, such as  $\zeta(f - f_0)\zeta^*(f - 2f_0)$ , vanish. As  $\zeta(f)$  is unknown [we can only estimate its PSD by Eq. (32)], here we show an example comparison between the simulated and experimentally measured  $S_{ii}|H(f)|^2$  to empirically demonstrate it to be a good approximation.

We estimate  $S_{\zeta\zeta}$  by the method described in Sec. III B with Eqs. (30)–(32) in a different STM setup, and the resulting PSDs are shown in Fig. 23.

Following Eq. (16), we can simulate  $S_{ii}$  of unfiltered lock-in demodulation signal with parameters  $I_{ac} = 10$  pA,  $I_{dc} = 1$  nA,

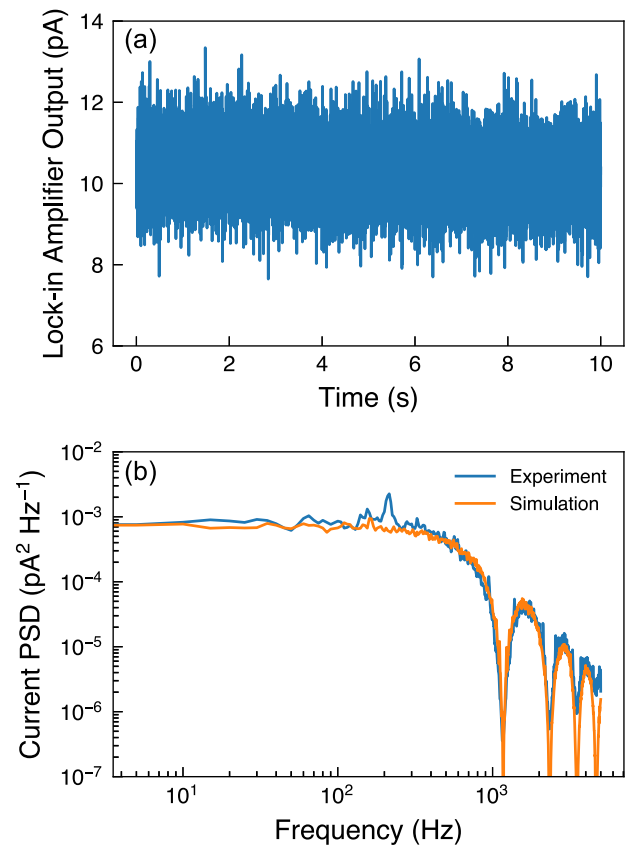


**FIG. 24.** Comparison between simulated and experimental noise current of the lock-in output. (a) Lock-in output measured by an oscilloscope (sampling rate 10 kHz) when the tip is in the tunneling range with feedback disabled and bias modulation activated. Setup conditions:  $V_{dc} = 0.4$  V,  $I_{dc} = 1.0$  nA,  $V_{ac} = 3.5$  mV, and  $f_0 = 1170$  Hz. (b) Simulated (orange) and experimental (blue) current PSD  $S_{ii}|H(f)|^2$  of the lock-in output. A simple boxcar filter with  $t_s = (2\pi f_0)^{-1}$  is applied after the lock-in demodulation. The experimental PSD is evaluated by Welch's method from (a), while the simulated PSD is calculated by applying the boxcar filter to  $S_{ii}$  estimated from Eq. (16).

$V_{dc} = 0.4$  V, and  $f_0 = 1170$  Hz. While the measurable PSD is the filtered lock-in demodulation signal, we apply a simple boxcar filter to  $S_{ij}$  as shown by the orange spectrum in Fig. 24(b). We measure the actual lock-in output with exactly the same parameters in the simulation in Fig. 24(a). The estimated PSD is shown by the blue spectrum in Fig. 24(b). The simulation agrees well with the experimental result, with an average underestimation of  $S_{ij}$  of 5%. This example indicates that Eq. (16) provides an excellent estimation of the noise PSD of the lock-in demodulation signal.

## REFERENCES

- <sup>1</sup>A. Selloni, P. Carnevali, E. Tosatti, and C. D. Chen, *Phys. Rev. B* **31**, 2602 (1985).
- <sup>2</sup>J. A. Stroschio, R. Feenstra, and A. Fein, *Phys. Rev. Lett.* **57**, 2579 (1986).
- <sup>3</sup>M. F. Crommie, C. P. Lutz, and D. M. Eigler, *Nature* **363**, 524 (1993).
- <sup>4</sup>Y. Hasegawa and P. Avouris, *Phys. Rev. Lett.* **71**, 1071 (1993).
- <sup>5</sup>J. Hoffman, K. McElroy, D.-H. Lee, K. Lang, H. Eisaki, S. Uchida, and J. Davis, *Science* **297**, 1148 (2002).
- <sup>6</sup>T. Hanaguri, C. Lupien, Y. Kohsaka, D.-H. Lee, M. Azuma, M. Takano, H. Takagi, and J. Davis, *Nature* **430**, 1001 (2004).
- <sup>7</sup>M. Allan, A. Rost, A. Mackenzie, Y. Xie, J. Davis, K. Kihou, C. Lee, A. Iyo, H. Eisaki, and T.-M. Chuang, *Science* **336**, 563 (2012).
- <sup>8</sup>D. Huang, C.-L. Song, T. A. Webb, S. Fang, C.-Z. Chang, J. S. Moodera, E. Kaxiras, and J. E. Hoffman, *Phys. Rev. Lett.* **115**, 017002 (2015).
- <sup>9</sup>J. Lee, M. Allan, M. Wang, J. Farrell, S. Grigera, F. Baumberger, J. Davis, and A. Mackenzie, *Nat. Phys.* **5**, 800 (2009).
- <sup>10</sup>A. R. Schmidt, M. H. Hamidian, P. Wahl, F. Meier, A. V. Balatsky, J. Garrett, T. J. Williams, G. M. Luke, and J. Davis, *Nature* **465**, 570 (2010).
- <sup>11</sup>B. B. Zhou, S. Misra, E. H. da Silva Neto, P. Aynajian, R. E. Baumbach, J. Thompson, E. D. Bauer, and A. Yazdani, *Nat. Phys.* **9**, 474 (2013).
- <sup>12</sup>G. M. Rutter, J. N. Crain, N. P. Guisinger, T. Li, P. N. First, and J. A. Stroschio, *Science* **317**, 219 (2007).
- <sup>13</sup>T. Zhang, P. Cheng, X. Chen, J.-F. Jia, X. Ma, K. He, L. Wang, H. Zhang, X. Dai, Z. Fang, X. Xie, and Q.-K. Xue, *Phys. Rev. Lett.* **103**, 266803 (2009).
- <sup>14</sup>H. Beidenkopf, P. Roushan, J. Seo, L. Gorman, I. Drozdov, Y. San Hor, R. J. Cava, and A. Yazdani, *Nat. Phys.* **7**, 939 (2011).
- <sup>15</sup>I. Zeljkovic, Y. Okada, C.-Y. Huang, R. Sankar, D. Walkup, W. Zhou, M. Serbyn, F. Chou, W.-F. Tsai, H. Lin, A. Bansil, L. Fu, M. Z. Hasan, and V. Madhavan, *Nat. Phys.* **10**, 572 (2014).
- <sup>16</sup>H. Zheng, G. Bian, G. Chang, H. Lu, S.-Y. Xu, G. Wang, T.-R. Chang, S. Zhang, I. Belopolski, N. Alidoust, D. S. Sanchez, F. Song, H.-T. Jeng, N. Yao, A. Bansil, S. Jia, H. Lin, and M. Z. Hasan, *Phys. Rev. Lett.* **117**, 266804 (2016).
- <sup>17</sup>L. Perfetti, P. Loukakos, M. Lisowski, U. Bovensiepen, H. Berger, S. Biermann, P. Cornaglia, A. Georges, and M. Wolf, *Phys. Rev. Lett.* **97**, 067402 (2006).
- <sup>18</sup>F. Schmitt, P. S. Kirchmann, U. Bovensiepen, R. G. Moore, L. Rettig, M. Krenz, J.-H. Chu, N. Ru, L. Perfetti, D. Lu, M. Wolf, I. Fisher, and Z. X. Shen, *Science* **321**, 1649 (2008).
- <sup>19</sup>Y. Wang, D. Hsieh, E. Sie, H. Steinberg, D. Gardner, Y. Lee, P. Jarillo-Herrero, and N. Gedik, *Phys. Rev. Lett.* **109**, 127401 (2012).
- <sup>20</sup>A. Damascelli, Z. Hussain, and Z.-X. Shen, *Rev. Mod. Phys.* **75**, 473 (2003).
- <sup>21</sup>C. Tusche, A. Krasnyuk, and J. Kirschner, *Ultramicroscopy* **159**, 520 (2015).
- <sup>22</sup>M. Lawler, K. Fujita, J. Lee, A. Schmidt, Y. Kohsaka, C. K. Kim, H. Eisaki, S. Uchida, J. Davis, J. Sethna *et al.*, *Nature* **466**, 347 (2010).
- <sup>23</sup>M. Hamidian, I. Fermo, K. Fujita, S. Mukhopadhyay, J. Orenstein, H. Eisaki, S. Uchida, M. Lawler, E. Kim, and J. Davis, *New J. Phys.* **14**, 053017 (2012).
- <sup>24</sup>The definitions in Eqs. (1) and (2) can be used for any signal of interest  $X(t)$ , with  $x(t)$  being its accompanying noise. In Sec. II, the signal of interest is the demodulated current measured at the output of the lock-in amplifier.
- <sup>25</sup>See <https://github.com/Let0n/achievinglownoiseinsts> for our interactive Python code.
- <sup>26</sup> $x(f)$  is commonly known as amplitude spectral density, and its unit is the unit of  $x(t)$  times  $\text{Hz}^{-1/2}$ .
- <sup>27</sup>A. Van der Ziel, *Proc. IEEE* **76**, 233 (1988).
- <sup>28</sup>P. H. Handel, *Phys. Rev. Lett.* **34**, 1492 (1975).
- <sup>29</sup>C. T. J. Alkemade, W. Snelleman, G. Boutilier, B. Pollard, J. Winefordner, T. Chester, and N. Omenetto, *Spectrochim. Acta, Part B* **33**, 383 (1978).
- <sup>30</sup>G. Boutilier, B. Pollard, J. Winefordner, T. Chester, and N. Omenetto, *Spectrochim. Acta, Part B* **33**, 401 (1978).
- <sup>31</sup>C. T. J. Alkemade, W. Snelleman, G. Boutilier, and J. Winefordner, *Spectrochim. Acta, Part B* **35**, 261 (1980).
- <sup>32</sup>The amplitude of the demodulating multiplier is set to unity here. If this amplitude is unknown in practice, the differential conductance  $g(V)$  can be normalized manually by the numerically differentiated  $I(V)$ .
- <sup>33</sup>This demodulation signal is normally inaccessible and not an actual output of the lock-in amplifier, but a mathematical result from the lock-in demodulation process. The actual accessible output of the lock-in amplifier is located after its LPF, as shown by  $I_{ac,x}$  and  $I_{ac,y}$  in Fig. 2(a).
- <sup>34</sup>The last term is calculated by Fourier transform of the square of  $I_{ac} \cos(4\pi f_0 t)$  in Eq. (10) to avoid ill-defined  $\delta^2(f \pm 2f_0)$ .
- <sup>35</sup>C. J. Chen, *Introduction to Scanning Tunneling Microscopy*, 2nd ed. (Oxford University Press, Oxford, 1993), Chap. 14.
- <sup>36</sup>D. White and J. Clare, *Meas. Sci. Technol.* **3**, 1 (1992).
- <sup>37</sup>E. Voigtman and J. D. Winefordner, *Rev. Sci. Instrum.* **57**, 957 (1986).
- <sup>38</sup>See <https://www.thinksrs.com/downloads/pdfs/catalog/SR556c.pdf> for specifications of the preamplifier.
- <sup>39</sup>P. Welch, *IEEE Trans. Audio Electroacoust.* **15**, 70 (1967).
- <sup>40</sup>S. Srinivasan, *Int. J. Electron.* **42**, 141 (1977).
- <sup>41</sup>G. De Geronimo, G. Bertuccio, and A. Longoni, *Rev. Sci. Instrum.* **67**, 2643 (1996).
- <sup>42</sup>See <http://www.ti.com/product/OPA827> for specifications of the opamp.
- <sup>43</sup>R. Mancini, *Op Amps for Everyone: Design Reference*, 2nd ed. (Newnes, Amsterdam, London, 2003), Chap. 8.
- <sup>44</sup>G. Giusi, G. Cannata, G. Scandurra, and C. Ciofi, *Int. J. Circuit Theory Appl.* **43**, 1455 (2015).
- <sup>45</sup>F. M. Klaassen and J. R. Robinson, *IEEE Trans. Electron Devices* **17**, 852 (1970).
- <sup>46</sup>S. S. Sesnic and G. R. Craig, *IEEE Trans. Electron Devices* **19**, 933 (1972).
- <sup>47</sup>J. T. Hastings and K. Ng, *Rev. Sci. Instrum.* **66**, 3691 (1995).
- <sup>48</sup>H. Birk, K. Oostveen, and C. Schönenberger, *Rev. Sci. Instrum.* **67**, 2977 (1996).
- <sup>49</sup>Z. Švindrych, Z. Janů, F. Soukup, and R. Tichý, *Cryogenics* **48**, 160 (2008).
- <sup>50</sup>C. Zhang, H. Jeon, M. Oh, M. Lee, S. Kim, S. Yi, H. Lee, I. Zoh, Y. Yoo, and Y. Kuk, *Rev. Sci. Instrum.* **88**, 066109 (2017).
- <sup>51</sup>A. T.-J. Lee, *Rev. Sci. Instrum.* **64**, 2373 (1993).
- <sup>52</sup>S. Urazhdin, S. Tessler, and R. Ashoori, *Rev. Sci. Instrum.* **73**, 310 (2002).
- <sup>53</sup>Y. J. Song, A. F. Otte, V. Shvarts, Z. Zhao, Y. Kuk, S. R. Blankenship, A. Band, F. M. Hess, and J. A. Stroschio, *Rev. Sci. Instrum.* **81**, 121101 (2010).
- <sup>54</sup>Q. Dong, Y. Liang, D. Ferry, A. Cavanna, U. Gennser, L. Couraud, and Y. Jin, *Appl. Phys. Lett.* **105**, 013504 (2014).
- <sup>55</sup>K. Rajagopalan, J. Abrokwhah, R. Droopad, and M. Passlack, *IEEE Electron Device Lett.* **27**, 959 (2006).
- <sup>56</sup>S. Oktyabrsky and D. Y. Peide, *Fundamentals of III-V Semiconductor MOSFETs* (Springer, 2010).
- <sup>57</sup>R. Terao, T. Kanazawa, S. Ikeda, Y. Yonai, A. Kato, and Y. Miyamoto, *Appl. Phys. Express* **4**, 054201 (2011).
- <sup>58</sup>Y. Xuan, Y. Q. Wu, H. C. Lin, T. Shen, and P. D. Ye, *IEEE Electron Device Lett.* **28**, 935 (2007).
- <sup>59</sup>I. Battisti, G. Verdoes, K. van Oosten, K. M. Bastiaans, and M. P. Allan, *Rev. Sci. Instrum.* **89**, 123705 (2018).
- <sup>60</sup>F. Masse, Q. Dong, A. Cavanna, Y. Jin, and M. Aprili, *Rev. Sci. Instrum.* **89**, 093708 (2018).
- <sup>61</sup>K. Bastiaans, T. Benschop, D. Chatzopoulos, D. Cho, Q. Dong, Y. Jin, and M. Allan, *Rev. Sci. Instrum.* **89**, 093709 (2018).
- <sup>62</sup>D. Rogovin and D. Scalapino, *Ann. Phys.* **86**, 1 (1974).
- <sup>63</sup>Here, we use the fact that  $I$  and  $V$  share the same sign, and  $\coth\left(\frac{eV}{2k_B T}\right)$  approaches  $V/|V|$  when  $V \rightarrow \pm\infty$ .

- <sup>64</sup>O. S. Lumbroso, L. Simine, A. Nitzan, D. Segal, and O. Tal, *Nature* **562**, 240 (2018).
- <sup>65</sup>I. Power and E. Society, in *IEEE Std 1143-2012 (Revision of IEEE Std 1143-1994)* (IEEE, 2013), p. 1.
- <sup>66</sup>E. B. Joffe and K.-S. Lock, *Grounds for Grounding: A Circuit to System Handbook* (John Wiley & Sons, 2011).
- <sup>67</sup>R. Morrison, *Grounding and Shielding: Circuits and Interference* (John Wiley & Sons, 2016).
- <sup>68</sup>N. Moussy, H. Courtois, and B. Pannetier, *Rev. Sci. Instrum.* **72**, 128 (2001).
- <sup>69</sup>I. Zeljkovic, D. Huang, C.-L. Song, B. Lv, C.-W. Chu, and J. E. Hoffman, *Phys. Rev. B* **87**, 201108 (2013).
- <sup>70</sup>N. D. Lang, *Phys. Rev. B* **37**, 10395 (1988).
- <sup>71</sup>J. Pitarke, P. Echenique, and F. Flores, *Surf. Sci.* **217**, 267 (1989).
- <sup>72</sup>M. Becker and R. Berndt, *Phys. Rev. B* **81**, 035426 (2010).
- <sup>73</sup>R. Smoluchowski, *Phys. Rev.* **60**, 661 (1941).
- <sup>74</sup>F. Tajaddodianfar, S. O. R. Moheimani, J. Owen, and J. N. Randall, *Rev. Sci. Instrum.* **89**, 013701 (2018).
- <sup>75</sup>L. Pabbi, A. Binion, R. Banerjee, B. Dusch, C. Shoop, and E. Hudson, *Rev. Sci. Instrum.* **89**, 063703 (2018).